nature astronomy

LETTERS

https://doi.org/10.1038/s41550-022-01640-z

Proton acceleration in thermonuclear nova explosions revealed by gamma rays

Classical novae are cataclysmic binary star systems in which the matter of a companion star is accreted on a white dwarf[1,2]. Accumulation of hydrogen in a layer eventually causes a thermonuclear explosion on the surface of the white dwarf[3], brightening the white dwarf to ~10^5 solar luminosities and triggering ejection of the accumulated matter. Novae provide the extreme conditions required to accelerate particles, electrons or protons, to high energies. Here we present the detection of gamma rays by the MAGIC telescopes from the 2021 outburst of RS Ophiuchi, a recurrent nova with a red giant companion, which allowed us to accurately characterize the emission from a nova in the 60 GeV to 250 GeV energy range. The theoretical interpretation of the combined Fermi LAT and MAGIC data suggests that protons are accelerated to hundreds of gigaelectronvolts in the nova shock. Such protons should create bubbles of enhanced cosmic ray density, of the order of 10 pc, from the recurrent novae.

A symbiotic nova can be formed when the companion star of the white dwarf (WD) is a red giant (RG)[4]. The ejecta of symbiotic novae expand within the dense wind of the RG companion. Nova outbursts usually last from weeks to months. While they are expected to repeat hundreds of times[5], the interval between consecutive events can be as long as hundreds of thousands of years[6]. However, a subclass of objects called recurrent novae allows us to observe such repeated outbursts over a human lifespan[7]. In our Galaxy, ten such objects are known in which the repetition of bursts has been seen within a century[6]. According to ref. [8], for the symbiotic nova to become recurrent, its WD must be massive ($\geq 1.1\,M_{\odot}$).

Novae have been deeply studied in the optical and X-ray ranges for decades[6,9–12], but only recently have they been shown to be emitters of high-energy gamma-ray radiation: first in the case of symbiotic novae[13] and soon after with classical novae[14]. Though this clearly indicates that charged particles are accelerated to high energies in novae, their nature and radiation mechanism are not yet clear. To understand the acceleration mechanism of high-energy particles, it is crucial to measure the maximum energies of the emitted radiation. Until recently, all spectra of gamma-ray novae have been measured only up to the 6–10 GeV range[14], with no hint of emission at higher energies[15,16].

RS Ophiuchi is a recurrent symbiotic nova with average time between major outbursts of 14.7 yr (ref. [6]). The most recent outburst, in August 2021, was promptly reported in optical[17] and high-energy (100 MeV < E < 10 GeV) gamma rays by the Large Area Telescope on board the Fermi Gamma-ray Space Telescope (Fermi LAT)[18]. The optical emission showed behaviour similar to that of the 2006 outburst (Extended Data Fig. 1). Following these alerts, MAGIC began observations of RS Oph as part of its nova follow-up programme[16], on 9 August 2021 at 22:27 UT, that is, about 1 d after the first optical and gigaelectronvolt detections. In parallel, the HESS Collaboration announced very-high-energy (VHE, $\gtrsim$100 GeV) gamma rays from RS Oph[19]. The MAGIC observations reveal VHE emission contemporaneous to the Fermi LAT and optical maxima, and a decrease below the VHE detection limit two weeks later (Fig. 1). Details of the analysis can be found in 'MAGIC' in Methods. The first 4 d of MAGIC observations (9–12 August) yield a VHE signal with a significance of 13.2σ (Extended Data Fig. 2), spanning from 60 GeV to 250 GeV, well fitted by a single power law ($\chi^2/N_{\rm dof} = 5.9/5$, where $N_{\rm dof}$ is the number of degrees of freedom).

Daily spectra are reconstructed (Extended Data Fig. 3, 'MAGIC' in Methods and Supplementary Section H), allowing us to track the evolution of the outburst.

The contemporaneous gamma-ray spectrum measured using Fermi LAT and MAGIC can be described as a single, smooth component spanning from 50 MeV to 250 GeV. Intriguingly, while the gigaelectronvolt emission subsides with a halving timescale of ~2.2 d (see also 'Fermi LAT' in Methods), the flux measured by MAGIC over the first 4 d is consistent with being constant ($\chi^2/N_{\rm dof} = 2.9/3$); see also Extended Data Fig. 4 This suggests a migration of the gamma-ray emission towards higher energies, in line with an increase of the maximum energies of the parent particles. RS Oph is the gamma-ray nova with the highest flux and energy output to date, as shown by the comparison with the other Fermi LAT-detected novae presented in Supplementary Section I. Therefore, the non-detection of previous novae in the VHE range[15,16] might be explained by the lack of sensitivity to dimmer eruptions, without the need to invoke any fundamental difference in the spectral energy distribution of RS Oph.

The conditions in novae are favourable for the acceleration and subsequent emission of radiation by both electrons and protons[14]. The expanding ejecta of a nova interacting with the interstellar medium (filled also with the dense RG wind in the case of symbiotic novae) will result in the formation of a shock wave. Moreover, the fast wind, induced by the nuclear burning on the surface of the WD, will catch up with the ejecta, causing an additional internal shock[20]. Recently, a correlation between optical and gamma-ray emission has further suggested that a substantial part of the novae explosion's power goes into shocks[21]. In such shocks, energetic electrons and protons can be produced (Fig. 2). Gamma-ray emission can arise from photosphere thermal radiation upscattered to the gamma-ray energy range by relativistic electrons via inverse Compton scattering. Alternatively, the ambient matter (nova ejecta and RG wind) can act as a target for hadronic interaction of protons or bremsstrahlung radiation of electrons[14]. The maximum energies of high-energy particles will depend on the efficiency of the acceleration mechanism, the duration of the nova and the cooling energy losses ('Acceleration and cooling of particles' in Methods and Extended Data Fig. 5). Protons experience only mild cooling by proton–proton interactions with a timescale of $t_{\rm pp} = 21(n_{\rm p}/6\times10^8\,{\rm cm^{-3}})^{-1}$ [d], where $n_{\rm p}$ is the number density of the target material. Electrons in nova shocks suffer stronger inverse Compton energy losses, with

A full list of authors and their affiliations appears at the end of the paper.

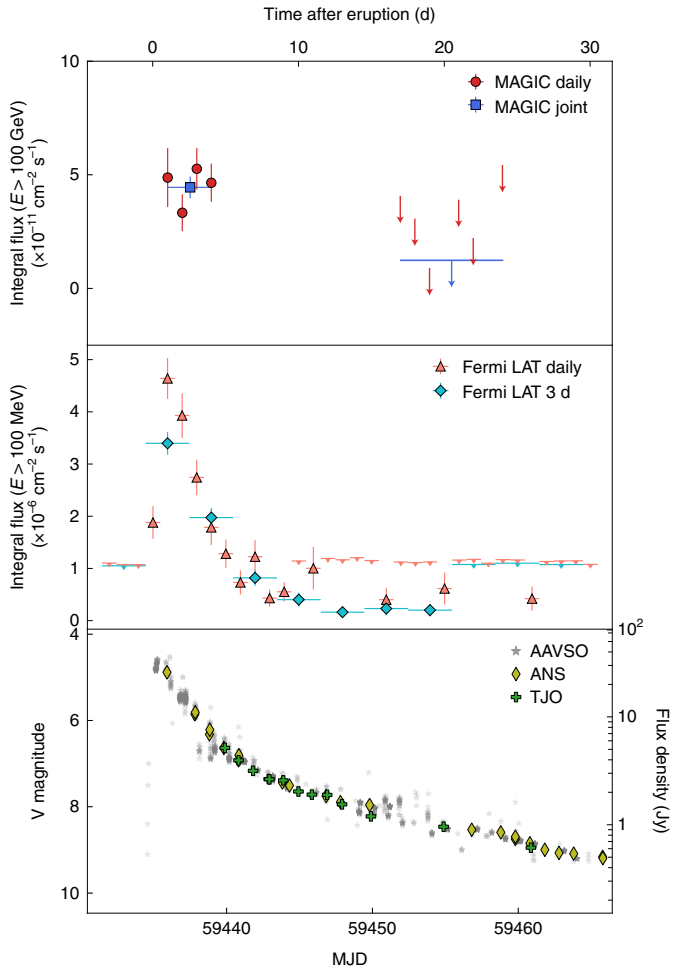

Fig. 1 | Multiwavelength light curve of RS Oph. The VHE (MAGIC, top), high-energy (Fermi LAT, middle) and optical (Joan Oró Telescope (TJO), Asiago Novae and Symbiotic Stars Collaboration (ANS) and American Association of Variable Star Observers International Database (AAVSO), bottom) bands. The lack of MAGIC data between MJD 59440 and MJD 59454 is due to the presence of bad weather conditions and strong moonlight. MJD, modified Julian date. Error bars represent 1σ statistical uncertainties in the data points, and arrows are 95% confidence level upper limits.

$t_{IC} = 4.4 \times 10^{-3} (E/300\,\mathrm{GeV})^{-1} [1 + 10(E/300\,\mathrm{GeV})]^{1.5}$ [d]. Therefore, the production of high-energy photons via leptonic mechanisms is much more demanding on the acceleration process efficiency than for proton models. The simultaneous acceleration of both types of particle (but reaching different energies) has also been proposed[16,22]. We estimate that bremsstrahlung is negligible with respect to the inverse Compton component for the parameters of RS Oph ('Modelling' in Methods).

We derive the photosphere parameters using fits to the photometry measurements (Extended Data Fig. 6) and shock expansion velocity from spectroscopy (Extended Data Fig. 7). On the basis of the optical observations of RS Oph during the 2021 outburst, and the derived parameters from previous outbursts of the source, we model the gamma-ray emission with the injection of a population of relativistic electrons or protons ('Modelling' in Methods). We take into account also the minor absorption of the emission in the photosphere radiation field (Extended Data Fig. 8). The Fermi LAT and MAGIC measurement can be well described ($\chi^2/N_{dof} = 13.1/12$, P value = 0.36) with the proton-only model (Fig. 3 left).

The fit yields a canonical power-law spectrum with an index of about −2 and an exponential cutoff, corresponding to the maximum energies achieved in the acceleration. The day-by-day modelling shows evidence that the energy cutoff of protons increases with time (Supplementary Section H and Extended Data Fig. 9). This is in line with the absence of spectral signatures from cooling terms. The associated neutrino emission is not expected to be detected by the current experiments (Supplementary Section F).

In contrast, it is difficult to explain the shape of the curvature of the measured spectrum between 50 MeV and 250 GeV with leptonic processes. The leptonic model requires injection of particles that already contain a strong break (change of particle index by 3.25 ± 0.28) in the electron energy distribution (Fig. 3 right). Since the break must already be present in the injection spectrum of particles, it cannot be explained by the cooling. In addition, despite a more complicated particle injection model, the description of the gamma-ray emission in the electron scenario is significantly worse ($\chi^2/N_{dof} = 27.5/11$, P value $= 3.9 \times 10^{-3}$) than in the case of protons, as can be seen in Fig. 3. The relative likelihood of the electron model with respect to the proton model for ΔAIC = 15.3, as defined within the Akaike information criterion framework[23], which is normally used for comparison of non-nested models, is 4.7×10^{-4}.

Despite their intense emission of gamma rays, accelerated protons will eventually escape the nova shock, carrying away most of their obtained energy. Such protons can contribute to the Galactic cosmic rays (CRs), which are expected to be produced mainly in supernova remnants[24].

The measurement of the proton spectrum required to explain the gamma-ray emission of RS Oph can be used to make estimates of the nova contribution to CRs. Using the CR energetics derived for RS Oph (~4.4×10^{43} erg, 'Energetics' in Methods), a rate of 50 novae yr^{-1} (ref. [25]) would lead to about 0.1% of the CR energy contribution from supernovae, which are rarer than novae (~2 per century) but much more energetic (~10^{50} erg). Despite the small contribution to the overall CR sea, a nova would notably increase the CR density in its close environment. The energy density of the nova dominates over that of the average CR energy density in the Milky Way (~1.8 eV cm^{-3}) in a region of radius ~0.5 pc, of the order of the distance to the nearest star in our Galaxy. In the special case of recurrent novae, protons accelerated over 10^5 yr (ref. [26]), assuming a recurrence rate of every 15 yr, will accumulate in a ~9 pc bubble with enhanced CR density ('Contribution to the CR sea' in Methods).

The detection of gamma rays reaching 250 GeV from a recurrent symbiotic nova allowed us to obtain a deep physical insight into the population of relativistic particles accelerated by such objects. The modelling of the gamma-ray spectrum strongly favours the explanation of the emission via the acceleration of protons in a nova shock. Evidence for the proton acceleration is based on (1) the inferred shape of the energy distribution of injected particles, (2) the better statistical description of the gamma-ray spectral energy distribution by the proton model and (3) the obtained evidence of the increase of the particle maximum energies over time, consistent with lack of strong cooling. The protons in the nova shock undergo slow cooling; therefore, they will eventually be able to escape the shock, carrying away a substantial fraction of energy. Such protons will add to the Galactic CR budget, but primarily in the close neighbourhood of novae.

The observation of the August 2021 outburst of RS Oph introduces a new class of sources as VHE gamma-ray emitters: (recurrent symbiotic) novae. RS Oph is a recurrent symbiotic nova, the same class of objects as V407 Cygni, the first nova detected in the gigaelectronvolt range by Fermi LAT. While we now know that classical novae are also gigaelectronvolt emitters, it remains to be seen if the detection of RS Oph emitting in the VHE gamma-ray range

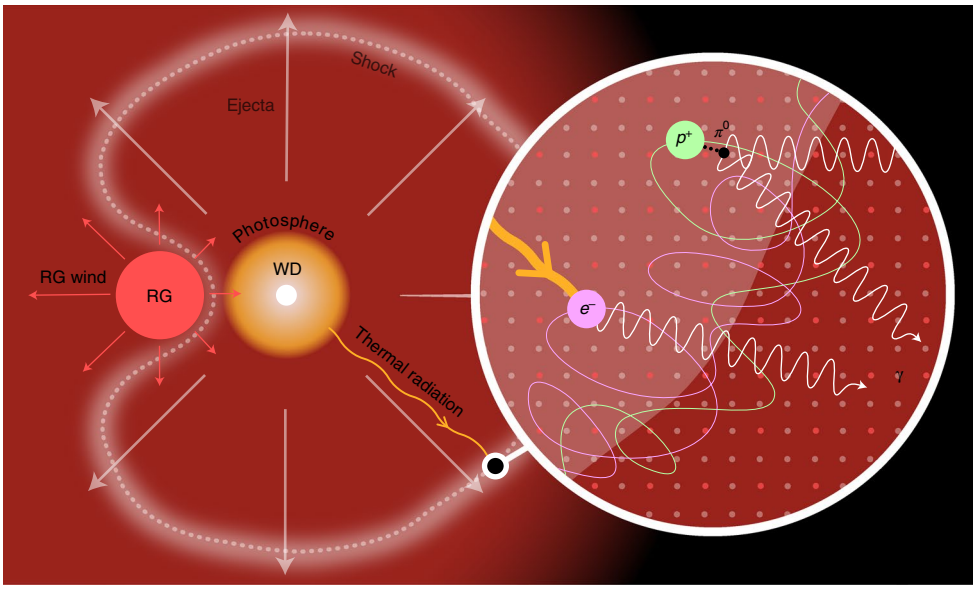

Fig. 2 | Schematic representation of RS Oph during an outburst. A photosphere (yellow circle) surrounds the WD (white small circle). Its companion star, an RG (red circle), emits a slow wind (red arrows). Ejecta of the nova explosion (grey arrows) propagate into the surrounding medium, causing a shock wave encompassing the binary system (grey dashed line). In the shock wave, energetic electrons and protons (magenta and green wavy lines, respectively) are trapped by a magnetic field and accelerated. Gamma rays (white arrows) are produced either by electrons scattering the thermal radiation of the photosphere (yellow arrow) or by protons interacting with the surrounding matter (grey and red dots).

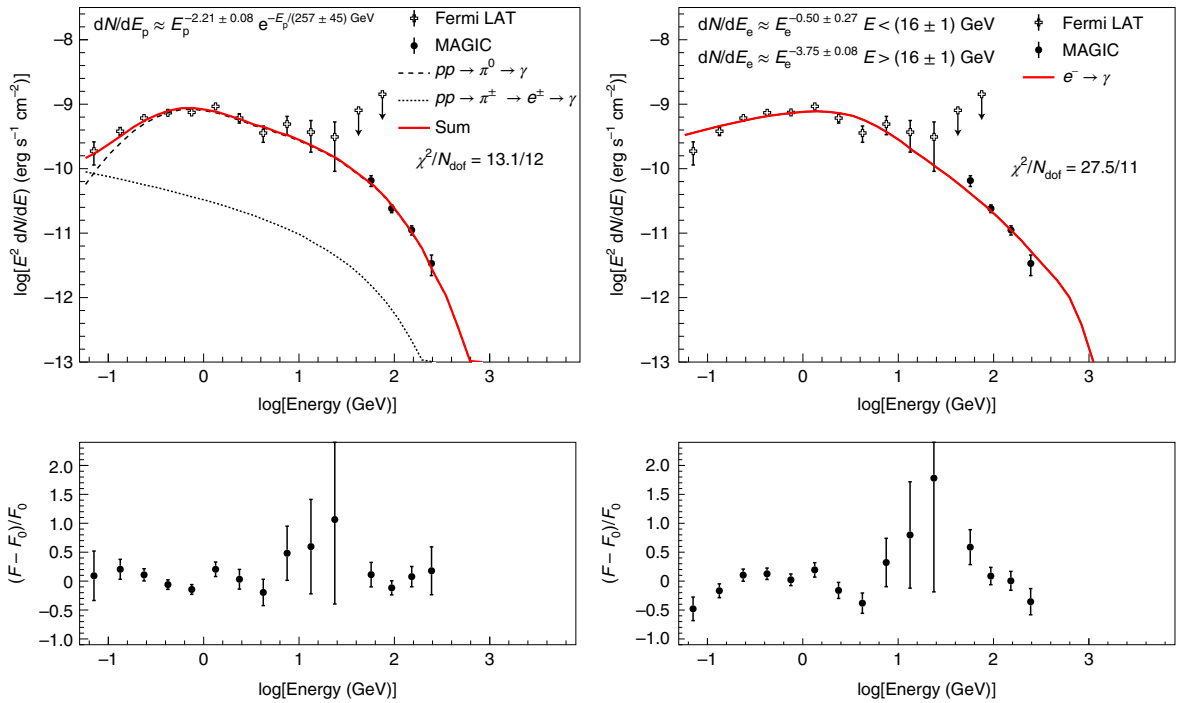

Fig. 3 | Gamma-ray spectrum of RS Oph observed over the first 4 d of the outburst, and modelled with both a hadronic and a leptonic scenario. Observations are averaged over the first 4 d of the outburst. Left: a hadronic model. Right: a leptonic model. The dashed line shows the gamma rays from the π^0 decay and the dotted line shows the inverse Compton contribution of the secondary $e^{\pm}$ pairs produced in hadronic interactions. dN/dE_p and dN/dE_e report the shapes of the proton and electron energy distributions obtained from the fit. Bottom: the fit residuals. Error bars represent 1σ statistical uncertainties in the data points.

is due to its recurrent symbiotic nature, or just the first sign of such emission from a broader class of classical novae. The comparison of gamma-ray measurements in gigaelectronvolt and VHE gamma-ray ranges with previous Fermi LAT novae does not reveal any peculiarity in the emission of RS Oph, except for its brightness (Fig. 4 and Extended Data Fig. 10). Therefore, it is likely that future, more sensitive VHE gamma-ray facilities will be able to provide an ample harvest of novae.

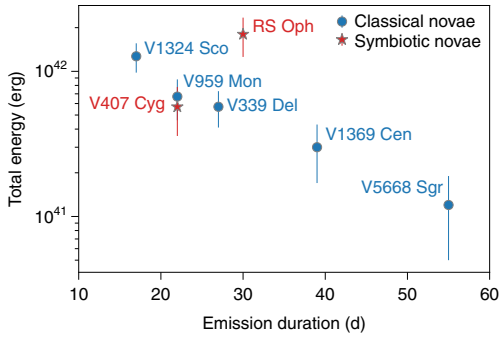

Fig. 4 | Total energy versus duration of RS Oph 2021 outburst compared with those of the other novae detected by Fermi LAT. Data taken from refs. [13,14,67]. Error bars represent 1σ statistical uncertainties in the data points.

Methods

Observations and data analysis. In this section we report the detailed results of the analysis of gamma-ray data with MAGIC and Fermi LAT, and optical data with TJO and ANS.

MAGIC. MAGIC[27] is a stereoscopic system of two imaging atmospheric Cherenkov telescopes situated in the Canary island of La Palma, Spain (28.8° N, 17.9° W at 2,225 m above sea level). Each telescope consists of a 17-m-diameter mirror dish and a fast imaging camera. The system achieves a sensitivity of (0.92 ± 0.04)% of the Crab Nebula flux above 210 GeV in 50 h in the zenith angle range 30–45° (ref. [28]).

MAGIC observed RS Oph in the period between 9 August 2021 and 1 September 2021 (MJD 59435.94 to 59458.97) for 34.0 h (Supplementary Table 2). The data quality selection was based on the atmospheric transmission and rates of background events. For this analysis we also did not include data taken under moonlight conditions, as they provide much higher energy threshold values. After quality cuts, 21.4 h of the data were used for the analysis, half of which were taken during the first 4 d after the nova eruption. The source was observed at zenith angles between 36° and 60°. The data were taken in the so-called wobble mode, pointing at four different sky positions situated 0.4° away from the source to evaluate the background simultaneously.

The data were analysed using the MAGIC Analysis and Reconstruction Software, MARS[29]. A dedicated low-energy procedure with a special signal extraction and image cleaning, the so-called MaTaJu method, was applied (see ref. [30] and references therein). Further processing of the data, including the image parameterization, the direction and energy reconstruction and gamma–hadron separation, was applied following the standard MARS analysis chain. The energy threshold of the analysis is ~60 GeV.

We fitted the spectrum obtained from the first 4 d of observations using a single power law ($dN/dE = f_0(E/E_0)^{-\alpha}$), resulting in a $\chi^2/N_{dof} = 5.9/5$ goodness of fit. The fit used also takes into account estimated energy bins without detected signal, hence the number of degrees of freedom is larger than expected from the number of points in the reconstructed spectrum. The normalization energy of the fit ($E_0 = 130$ GeV) is the decorrelation energy (that is, normalization energy that minimizes the correlation of the fit parameters) of the 4 d sample. The fit parameters are listed in Supplementary Table 3.

To estimate the lower limit on the maximal true energy of gamma rays consistent with the MAGIC data we follow the procedure of ref. [31]. We perform a likelihood fit of the data with a power-law model with a sharp cutoff at a given energy E_{cut}. The 3σ (99.7% confidence level) lower limit on E_{cut} is the value for which the increase of the χ^2 of the fit is equal to 9. We obtain 170 GeV; however, taking into account also the 15% systematic uncertainty on the energy scale following ref. [29] we obtain a slightly less constraining, conservative limit of $E_{cut} > 150$ GeV.

We have also performed night-by-night spectral fits to investigate spectral variability. The parameters from the first two nights are consistent within errors (note however that the exposure is lower on the first night than on the remaining ones). A hint of hardening of the emission is seen between the second and the third night. No significant change of parameters can be seen between the third and the fourth night.

The daily-binned light curve was calculated for an integral flux above 100 GeV. For the first 4 d, the fit to a constant flux gives a $\chi^2/N_{dof} = 2.9/3$ with a value of $F_0 = (4.41 \pm 0.46_{stat}) \times 10^{-11}\,cm^{-2}\,s^{-1}$.

Fermi LAT. Fermi LAT is a pair conversion telescope designed to detect gamma rays with an energy range from 0.02 GeV to >300 GeV (ref. [32]). With its large field of view (2.4 sr), it observes the entire sky approximately every 3 h. Each analysis is performed with fermitools v2.0.8 and Fermipy v1.0.2[33] using a binned likelihood analysis, P8R3_V3 instrument response functions and the catalogue 4FGL-DR2[34,35] with the standard Galactic and isotropic diffuse background to construct the model of the region of interest (ROI). For each analysis, the SOURCE event class is used, as this is the recommended event class for long-duration observations (observations of more than a few hours). The SOURCE event class can be further divided into separate event types such as PSF0, PSF1, PSF2 and PSF3, where PSF0 corresponds to events with the worst point spread function (PSF) and PSF3 are events with the best PSF.

For the 1 d and 3 d time bins, the Fermi LAT dataset used encompasses a total time range from MJD 59431.45 to 59461.45, an energy range from 0.1 GeV to 1,000 GeV and a 15° ROI centred on the radio coordinates of RS Oph (RA = 267.555°, dec. = −6.7078°). We use event type 3, which corresponds to all events, for this analysis and select a maximum zenith angle of >90° to reduce any gamma-ray contamination from the Earth limb. The majority of 4FGL-DR2 sources for the 1 d and 3 d time bins are not significantly detected (test statistic (TS) > 25, ref. [36]), apart from 4FGL J1813.4-1246 and 4FGL J1745.4-0753. These sources correspond to PSR J1813-1246 and TXS 1742-078, which are 8.3° and 1.7° away from RS Oph. Here, TS is defined as $TS = -2\ln(\mathcal{L}_{max,0}/\mathcal{L}_{max,1})$, where $\mathcal{L}_{max,0}$ is the maximum likelihood of the null hypothesis and $\mathcal{L}_{max,1}$ is the maximum likelihood with the source included[36]. The square root of the TS is approximately equal to the significance of detection, that is, a TS of 25 is ~5σ. TXS 1742-078 is a non-variable hard blazar and therefore could cause possible source confusion. Due to the proximity of 4FGL J1745.4-0753 to RS Oph and possible source confusion at the lowest energies, the value of the index of 4FGL J1745.4-0753 is locked to that of the 4FGL-DR2 catalogue. RS Oph is included in the ROI and modelled with a log parabola model. Additional spectral models were tested for a 4 d period contemporaneous to MAGIC observations—a power law (TS = 2,168.1) as well as a power law with an exponential cutoff (TS = 2,016.4)—and the log parabola model (TS = 2,226.44) had the highest TS; therefore, we use the log parabola model as our spectral form for RS Oph. The ROI is optimized with the normalization and spectral parameters of any 4FGL-DR2 source with a number of predicted counts of <1 locked to the 4FGL-DR2 values, excluding the Galactic and isotropic diffuse background. All parameters on all unlocked 4FGL-DR2 sources within 4° are left free to vary, and the ROI is fitted using the Minuit minimizer. If the RS Oph source model does not have TS > 9 or a number of predicted counts of >4, or the error of the integrated flux from 0.1 GeV to 1,000 GeV is greater than 60% of the value, then it is not considered detected and 95% upper limits are calculated. These 1 d and 3 d light curves are presented in Supplementary Tables 4 and 5 and in Fig. 1. The 1 d light curve in the MJD 59435.45–59444.45 range can be well fitted ($\chi^2/N_{dof} = 6.5/7$) with an exponential decay with halving time of (2.20 ± 0.18) d.

The analysis of the combined first four days has a dataset that encompasses a time range MJD 59435.45–59439.45 and an energy range from 0.05 GeV to 1,000 GeV. Reaching 0.05 GeV is necessary to help distinguish the leptonic and hadronic models described in the main text and seen in Fig. 3. The same procedure is applied as in the 1 d and 3 d time bins, with some adjustments in the settings to allow the analysis to reach 0.05 GeV. Due to the worsening of the Fermi LAT PSF below 0.1 GeV, we apply a 20° ROI centred on RS Oph, and a more restrictive zenith angle selection of >80°. We perform a joint-likelihood analysis with two components, one in the energy range from 0.05 GeV to 0.1 GeV and one in the energy range from 0.1 GeV to 1,000 GeV. We remove PSF0 and PSF1 event types from the analysis below 0.1 GeV and retain all event types above 0.1 GeV. PSF0 and PSF1 are events classified with poor PSF, and removing these event types therefore improves the PSF with the trade-off of fewer data. This reduces the possibility of source confusion from nearby weak sources. It also reduces the chance of false positive detections as described in the Fermi LAT low-energy catalogue[37].

Optical photometry. Optical photometric observations of RS Oph were carried out using TJO and ANS (telescopes ID 310, 610 and 2203). The TJO is a 1-m-class robotic telescope located at Montsec Observatory (42.05° N, 0.73° E), Catalonia, Spain. The multi band (BVR_cI_c) data were analysed using a semiautomatic pipeline for differential photometry[38] assuming the aperture radius of 7.5″. The comparison star magnitudes are obtained from AAVSO. The stars are numbered 115, 121, 129, 130 and 133 in the database finding chart.

The data obtained with ANS are analysed using PSF photometry method described in refs. [39,40]. The same local photometric sequence, extracted from the AAVSO All-Sky Photometric Survey (APASS) DR8[41,42] and accurately placed on the system of equatorial standards[43] via the colour equations calibrated in refs. [44,45], has been used for all telescopes, ensuring a high consistency of the data. The photometry results are given in Supplementary Table 6, where the quoted uncertainties are the total error, which quadratically combine the measurement error on the variable with the error associated with the transformation from the instantaneous local photometric system to the standard one (as defined by the photometric comparison sequence). All measurements were carried out with aperture photometry.

The cross-calibration between instruments was performed by using the colour index of the source. The data obtained using the two telescopes are in good agreement. However, to reduce the systematic uncertainties, minimal offsets ($B - V = +0.03$, $V - R_c = +0.05$ and $V - I_c = -0.02$) were applied to TJO data. The contributions of the strongest emission lines (Hα and Hβ) were removed from

the observed magnitude using the simultaneous spectroscopic observations from the publicly available optical spectra in the Astronomical Ring for Amateur Spectroscopy (ARAS)[46]. We found that the contribution of the Hβ emission line in the V band is negligible for the first 10 d after the outburst. The contribution of the Hβ emission line is important in the B band and increases from 3% to 15% during the same time interval. Moreover, the contribution of the Hα emission line is dominant in the R band and increases from 5% to 83% during the same time interval owing to a sudden jump from 5% to 34% between $T-T_0=0.98$ d and $T-T_0=2.89$ d. The results of these corrections are presented in Supplementary Table 7.

All optical data described in this section are corrected for the effect of Galactic extinction by assuming $E(B-V)=0.65$ (ref. [47]), the Galactic extinction law[48] and the absolute fluxes (corresponding to zero magnitude)[49] in each band.

During the nova outburst the photosphere emission creates the dominant radiation field. We describe the radiation field using photometric and spectroscopic measurements by applying the black-body approximation. During the first 4 d of the nova, contemporaneous with the MAGIC measurements, the emission can be described by the photosphere temperature dropping from $T_{\rm ph}=10{,}800$ K to 7,680 K and radius $R_{\rm ph}=200\,R_\odot$ (Extended Data Fig. 6). It should be noted that the asymmetry of the photosphere (see, for example, refs. [50,51]), lack of measurements at the shortest wavelengths and the presence of lines affect the above-mentioned fits. Therefore, the photosphere radius and temperature values should be considered only a crude approximation of the radiation field, in the context of gamma-ray emission, and no conclusion on the evolution of these two parameters should be drawn. Note that the photosphere fit of the 2006 eruption[51], when rescaled to the nova distance of $d=2.45$ kpc, provides a similar radius (245–310) $R_\odot$ and temperature (8,200 K).

Spectroscopy and ejecta kinematics. RS Oph spectra during the 2021 outburst have been acquired with the Echelle spectrograph of the Varese 0.84 m telescope[52] and the Catania Astrophysical Observatory Spectropolarimeter[53] of the Catania 0.91 m telescope. The reduction of spectra, which included the subtraction of the bias frame, trimming, correcting for the flat-field and the scattered light, extraction for the orders, and wavelength calibration, was done as in ref. [54] using the IRAF (Image Reduction and Analysis Facility) packages. IRAF is distributed by the National Optical Astronomy Observatory, which is operated by the Association of Universities for Research in Astronomy, Inc.

The Hα profile obtained on day $T-T_0=0.91$ consists of a triangular shape with full-width at zero intensity of ~7,500 km s^{-1} and a blueshift absorption component at 4,250 km s^{-1}, exactly as reported in ref. [55] 1.38 d after the 2006 outburst of RS Oph.

The close similarity of the 2006 and 2021 spectral line profiles along the envelope expansion is testified on day $T-T_0=15$ by the presence of satellite components at the same high velocity (2,500 km s^{-1}). This feature was associated in ref. [55] with the presence of two jets (compare Figs. 1 and 2 therein and Extended Data Fig. 7). Also, ref. [56] reported a measured velocity of 4,200 km s^{-1} the day after the outburst.

Because of the day-by-day changes of absorption and emission features across the whole RS Oph spectrum, we have determined the velocity of the expanding envelope as the terminal value simultaneously representative of the Hα, Hβ and He I λ5876 P Cygni profiles (Supplementary Table 8). An error of 250 km s^{-1} was assumed as representative of differences between profiles. Extended Data Fig. 7 shows these profiles in the first three days after the expansion as well as on days 5 and 15.

The acceleration along the initial 3 d is not statistically confirmed and we assume (4,500 ± 250) km s^{-1} as representative of the ejecta expansion at the earliest stage (during the VHE gamma-ray detection by MAGIC).

It is worth recalling that this velocity is a volume average, weighted by the brightness, temperature and density of the ejecta velocities, and agrees with results from the modelling in ref. [57] of the HST images of the spatially resolved and expanding ejecta during the 2006 event. Radio maps of the 2006 outburst of RS Oph[58] have shown the presence of highly collimated flows with a velocity close to 10,000 km s^{-1}. In this framework, the decrement of the velocity after the initial days is simply a consequence of a non-spherical mass outflow[55,57,59].

Modelling. There is compelling evidence, both simulation (see, for example, ref. [60]) and observational (see, for example, ref. [59]), that the mass transfer in symbiotic binaries causes a non-spherical circumstellar environment. Such asymmetries are crucial when considering the morphology of the emission in particular in optical and X-ray ranges. Here, using a similar approach to refs. [16,22], we consider a simplified, spherically symmetric scenario to evaluate the conditions in which gamma-ray radiation can be produced by either electrons or protons and to investigate spectral features of such an emission. The parameters used are summarized in Supplementary Table 10.

Acceleration and cooling of particles. We parametrize the acceleration of charged particles with acceleration parameter ξ:

$$\left(\frac{{\rm d}E}{{\rm d}t}\right)_{\rm acc} = \frac{\xi cE}{R_{\rm L}(E)}, \tag{1}$$

where $R_{\rm L}(E)$ is the Larmor radius of a particle with energy E in perpendicular magnetic field B. The corresponding acceleration timescale can be computed as

$$t_{\rm acc} = E/\left(\frac{{\rm d}E}{{\rm d}t}\right)_{\rm acc} = 3.9\left(\frac{E}{300\,{\rm GeV}}\right)\left(\frac{\xi B}{10^{-7}\,{\rm G}}\right)^{-1}\,[{\rm d}]. \tag{2}$$

The maximum achieved energies will stem from balancing this acceleration time with ballistic time $t_{\rm bal}$, defined as the time from the onset of the nova, or by a dominating cooling process. The shock distance $R_{\rm sh}$ at the time $t=T-T_0$ can be estimated on the basis of its speed $v_{\rm sh}$:

$$R_{\rm sh} = 1.2\times10^{14}\left(\frac{v_{\rm sh}}{4{,}500\,{\rm km\,s^{-1}}}\right)\left(\frac{t}{3\,{\rm d}}\right)\,[{\rm cm}]. \tag{3}$$

As the nova shock expands, the adiabatic energy losses will be directly connected with the ballistic time. We define the adiabatic timescale as the time in which the energy of particles decreases by a factor of e, resulting in $t_{\rm adiab}=et_{\rm bal}$.

The protons will cool on hadronic interactions with the ambient matter, either the nova ejecta or the RG wind. We assume that the ejecta concentrate at the distance of $R_{\rm sh}$ in a layer with a thickness of $hR_{\rm sh}$, with $h=0.1$. The number density of the ejecta can be estimated as

$$\begin{aligned} n_{\rm ej} &= \frac{M_{\rm ej}}{4\pi hR_{\rm sh}^3 m_{\rm p}} \\ &= 6.0\times10^8\,\frac{M_{\rm ej}}{10^{-6}\,M_\odot}\left(\frac{v_{\rm sh}}{4{,}500\,{\rm km\,s^{-1}}}\right)^{-3}\left(\frac{t}{3\,{\rm d}}\right)^{-3}\left(\frac{h}{0.1}\right)^{-1}\,[{\rm cm^{-3}}], \end{aligned} \tag{4}$$

where $M_{\rm ej}$ is the total ejected mass and $m_{\rm p}$ is the proton mass. An alternative assumption that the ejecta fill homogeneously a sphere with radius $R_{\rm sh}$ would result in a value of $n_{\rm ej}$ lower by a factor of 3. The number density of the ambient material in the RG wind can be estimated as

$$\begin{aligned} n_{\rm RG} &= \frac{\dot{M}_{\rm RG}}{4\pi R_{\rm sh}^2 v_{\rm RG} m_{\rm p}} \\ &= 1.1\times10^8\,\frac{\dot{M}_{\rm RG}}{5\times10^{-7}\,M_\odot\,{\rm yr^{-1}}}\left(\frac{v_{\rm sh}}{4{,}500\,{\rm km\,s^{-1}}}\right)^{-2}\left(\frac{t}{3\,{\rm d}}\right)^{-2}\left(\frac{v_{\rm RG}}{10\,{\rm km\,s^{-1}}}\right)^{-1}\,[{\rm cm^{-3}}], \end{aligned} \tag{5}$$

where $v_{\rm RG}$ is the speed of the RG wind and $\dot{M}_{\rm RG}$ is the mass loss rate of the RG. The total density of the ambient medium for the hadronic interaction for the assumed parameters of RS Oph is mostly dominated by the ejecta ($n_{\rm p}\approx n_{\rm ej}$). The proton cooling timescale on hadronic p–p interactions can be then computed as

$$t_{\rm pp} = (n_{\rm p}c\sigma_{\rm pp})^{-1} = 21(n_{\rm p}/6\times10^8\,{\rm cm^{-3}})^{-1}\,[{\rm d}], \tag{6}$$

where $\sigma_{\rm pp}=3\times10^{-26}$ cm^2. As the cooling timescale is longer than the ballistic time, the maximum energies to which protons can be accelerated are determined by the time from the nova onset.

In the case of electrons, cooling losses can originate either from inverse Compton scattering on the photosphere thermal radiation or from bremsstrahlung radiation on the ambient matter. We compute the inverse Compton cooling timescale taking into account the Klein–Nishina correction factor following ref. [61]:

$$t_{\rm IC} = \frac{3(m_{\rm e}c^2)^2}{4c\sigma_T u_{\rm ph}E}\left(1+4\epsilon_{\rm ph}E/(m_{\rm e}c^2)^2\right)^{1.5}, \tag{7}$$

where $m_{\rm e}$ is the electron mass. The total energy density, $u_{\rm ph}$, and characteristic temperature of soft photons, $\epsilon_{\rm ph}$, can be estimated as

$$u_{\rm ph} = 0.14\,\frac{(R_{\rm ph}/200\,R_\odot)^2(T_{\rm ph}/8{,}460\,{\rm K})^4}{(v_{\rm sh}/4{,}500\,{\rm km\,s^{-1}})^2(t/3\,{\rm d})^2}\,[{\rm erg\,cm^{-3}}] \tag{8}$$

$$\epsilon_{\rm ph} = 2.2(T_{\rm ph}/8{,}460\,{\rm K})\,[{\rm eV}]. \tag{9}$$

For the scaling values used above the dependence of $t_{\rm IC}$ on energy can be given as $t_{\rm IC}=4.4\times10^{-3}(E/300\,{\rm GeV})^{-1}[1+10(E/300\,{\rm GeV})]^{1.5}$ [d], resulting in fast cooling of high-energy electrons. We estimate the bremsstrahlung losses using the same density of ambient matter $n_{\rm p}$ as

$$t_{\rm brems} = X_0/(n_{\rm p}m_{\rm p}c) = 24(n_{\rm p}/6\times10^8\,{\rm cm^{-3}})^{-1}\,[{\rm d}], \tag{10}$$

where $X_0=63$ g cm^{-2} is the radiation length in the proton gas. For the expected parameters of RS Oph, the bremsstrahlung losses are thus negligible. The synchrotron energy losses are also negligible, unless the magnetic field in the shock reaches the level of about 1 G.

To accelerate protons up to energies of a few hundred gigaelectronvolts, a value of $\xi B\gtrsim10^{-7}$ G is required (Extended Data Fig. 5). If electrons are accelerated in the same conditions, they can reach energies of only ~10 GeV. To explain the observed

gamma-ray emission reaching hundreds of gigaelectronvolts, much higher values, $\xi B \gtrsim 3\times10^{-6}$ G, are required. Second-order Fermi acceleration on the nova shock is expected to provide an acceleration parameter of the order of $\xi \lesssim (v_{sh}/c)^2 \approx 10^{-4}$, resulting in the requirement of $B \gtrsim 0.03$ G fields for the electron case and the much weaker $B \gtrsim$ mG for the proton one.

Energetics. The kinetic energy of the ejecta can be estimated as

$$E_k = 0.5 M_{ej} v_{sh}^2 = 2.0 \times 10^{44} \left(\frac{M_{ej}}{10^{-6}\,M_\odot}\right)\left(\frac{v_{sh}}{4{,}500\ \mathrm{km\ s^{-1}}}\right)^2 \mathrm{erg}. \quad (11)$$

For the assumed parameters determining the density of target material, the fit of the proton energy distribution in Fig. 3 requires a total power in protons of 4.4×10^{43} erg. This energetics requirement scales with the assumed model parameters as

$$E_{p,nova} = 0.44 \times 10^{44} \left(\frac{M_{ej}}{10^{-6}\,M_\odot}\right)^{-1}\left(\frac{v_{sh}}{4{,}500\ \mathrm{km\ s^{-1}}}\right)^{3}\left(\frac{d}{2.45\ \mathrm{kpc}}\right)^{-2}\frac{h}{0.1}\ \mathrm{erg}. \quad (12)$$

Therefore the efficiency of conversion of energy from the shock to protons can be computed as

$$\epsilon = \frac{E_{p,nova}}{E_k} = 0.22\left(\frac{M_{ej}}{10^{-6}\,M_\odot}\right)^{-2}\left(\frac{v_{sh}}{4{,}500\ \mathrm{km\ s^{-1}}}\right)\left(\frac{d}{2.45\ \mathrm{kpc}}\right)^{-2}\frac{h}{0.1}. \quad (13)$$

It is clear that protons need to obtain a substantial fraction (~20%) of the shock kinetic energy. A lower fraction can be achieved if the mass of the ejecta is higher, it is more concentrated at the shock (lower h) or the speed of the shock is decreased. Concentration of the nova ejecta and proton acceleration in the bipolar direction would increase the target material density and efficiency of the gamma-ray production. This would further lower the total energy required in the accelerated protons compared with the spherically symmetric scenario assumed here.

Contribution to the CR sea. These accelerated protons eventually escape the nova to be part of the sea of CRs. Since they do not suffer strong energy losses due to their interaction with intergalactic magnetic and photon fields, as is the case for electrons, their contribution may extend to large distance from the nova explosion at all energies. Assuming that the energy released in all novae into accelerated protons is similar to that released in RS Oph ($E_{p,nova} = 4.4\times10^{43}$ erg) and a nova rate of ~50 yr^{-1} (ref. [25]), we obtain a total of

$$\text{Nova energy rate} = E_{p,nova} \times \text{Nova rate} = 2.2 \times 10^{45}\ [\mathrm{erg\ yr^{-1}}]. \quad (14)$$

It is considered that a supernova explosion usually releases $E_{SN} \approx 10^{51}$ erg (ref. [62]), of which ~10% can be converted into accelerated protons at the shock between the supernova ejecta and the interstellar medium. The supernova rate in the Galaxy is ~2 per century[63]; therefore, the supernova energy rate would be

$$\text{Supernova energy rate} = 0.1 E_{SN} \times \text{Supernova rate} = 2 \times 10^{48}\ [\mathrm{erg\ yr^{-1}}], \quad (15)$$

making the contribution of novae $\lesssim$0.2% of that of supernovae.

Let us now assume that the average energy density in CRs in the Milky Way is $E_{dens,CRs} \approx 1.8\ \mathrm{eV\ cm^{-3}}$ (ref. [64]). We would like to compute the region in which the energy density of the protons accelerated by the nova dominates over this energy density. The energy density of these protons will be given by the total energy ($E_{p,nova}$) divided by the volume of the region

$$E_{dens,nova,1\ eruption} = \frac{3E_{p,nova}}{4\pi R_{eruption}^3}, \quad (16)$$

where $R_{eruption}$ is the radius of the region. If we compare $E_{dens,nova} = E_{dens,CRs}$, we obtain $R_{eruption} \approx 0.5$ pc, which is subject to the assumption on the energy density performed and may change if higher energy densities are considered[65].

Finally, in the special case of a recurrent nova such as RS Oph that repeats its explosions every ~15 yr (ref. [66]), we would obtain this energy injection repeated over time. Considering a period of recurrence of up to 10^5 yr, the region over which this nova would dominate has a size of

$$E_{dens,nova,recurrent} = \frac{3E_{p,nova} \times 10^4}{4\pi R_{recurrent}^3} \quad (17)$$

and the radius over which the protons accelerated by the nova would dominate over the energy density of the interstellar medium would be $R_{recurrent} \approx 9$ pc.

Data availability

Analysis products of MAGIC data are available at http://vobs.magic.pic.es/fits/. Low-level data are available on request.

Code availability

The code for fitting the electron and proton models is available at https://opendata.magic.pic.es/download?pid=2.

Received: 9 November 2021; Accepted: 22 February 2022;
Published online: 14 April 2022

References

1. Bode, M. F. & Evans, A. *Classical Novae* Vol. 43 (Cambridge Univ. Press, 2008).
2. Chomiuk, L., Metzger, B. D. & Shen, K. J. New insights into classical novae. *Annu. Rev. Astron. Astrophys.* **59**, 391–444 (2021).
3. Townsley, D. M. & Bildsten, L. Theoretical modeling of the thermal state of accreting white dwarfs undergoing classical nova cycles. *Astrophys. J.* **600**, 390–403 (2004).
4. Mikołajewska, J. Symbiotic stars: observations confront theory. *Balt. Astron.* **21**, 5–12 (2012).
5. Ford, H. C. The number of outbursts of a classical nova. *Astrophys. J.* **219**, 595–596 (1978).
6. Schaefer, B. E. Comprehensive photometric histories of all known Galactic recurrent novae. *Astrophys. J. Suppl. Ser.* **187**, 275–373 (2010).
7. Webbink, R. F., Livio, M., Truran, J. W. & Orio, M. The nature of the recurrent novae. *Astrophys. J.* **314**, 653–672 (1987).
8. Mikolajewska, J. The place of recurrent novae among the symbiotic stars. In *RS Ophiuchi (2006) and the Recurrent Nova Phenomenon* (eds Evans, A. et al.) 42 (Astronomical Society of the Pacific Conference Series Vol. 401, 2008).
9. Sokoloski, J. L., Luna, G. J. M., Mukai, K. & Kenyon, S. J. An X-ray-emitting blast wave from the recurrent nova RS Ophiuchi. *Nature* **442**, 276–278 (2006).
10. Bode, M. F. et al. Swift observations of the 2006 outburst of the recurrent nova RS Ophiuchi. I. Early X-ray emission from the shocked ejecta and red giant wind. *Astrophys. J.* **652**, 629–635 (2006).
11. Ness, J.-U. et al. The SSS phase of RS Ophiuchi observed with Chandra and XMM-Newton. I. Data and preliminary modeling. *Astrophys. J.* **665**, 1334–1348 (2007).
12. Nelson, T. et al. X-ray spectroscopy of the 2006 outburst of RS Ophiuchi. *Astrophys. J.* **673**, 1067–1079 (2008).
13. Abdo, A. A. et al. Gamma-ray emission concurrent with the nova in the symbiotic binary V407 Cygni. *Science* **329**, 817–821 (2010).
14. Ackermann, M. et al. Fermi establishes classical novae as a distinct class of gamma-ray sources. *Science* **345**, 554–558 (2014).
15. Aliu, E. et al. VERITAS observations of the nova in V407 Cygni. *Astrophys. J.* **754**, 77 (2012).
16. Ahnen, M. L. et al. Very high-energy γ-ray observations of novae and dwarf novae with the MAGIC telescopes. *Astron. Astrophys.* **582**, A67 (2015).
17. Geary, K. Outburst of RS Ophiuchi. *VSNET-alert* 26131 (2021).
18. Cheung, C. C., Ciprini, S. & Johnson, T. J. Fermi-LAT gamma-ray detection of the recurrent nova RS Oph. *The Astronomer's Telegram* **14834** (2021).
19. Wagner, S. J. & HESS Collaboration Detection of VHE gamma-ray emission from the recurrent nova RS Ophiuchi with HESS. *The Astronomer's Telegram* 14844 (2021).
20. Martin, P., Dubus, G., Jean, P., Tatischeff, V. & Dosne, C. Gamma-ray emission from internal shocks in novae. *Astron. Astrophys.* **612**, A38 (2018).
21. Aydi, E. et al. Direct evidence for shock-powered optical emission in a nova. *Nat. Astron.* **4**, 776–780 (2020).
22. Sitarek, J. & Bednarek, W. GeV–TeV gamma rays and neutrinos from the nova V407 Cygni. *Phys. Rev. D* **86**, 063011 (2012).
23. Akaike, H. A new look at the statistical model identification. *IEEE Trans. Autom. Control* **19**, 716–723 (1974).
24. Metzger, B. D. et al. Novae as tevatrons: prospects for CTA and IceCube. *Mon. Not. R. Astron. Soc.* **457**, 1786–1795 (2016).
25. Shafter, A. W. The Galactic nova rate revisited. *Astrophys. J.* **834**, 196 (2017).
26. Bath, G. T. & Shaviv, G. The space density, recurrence rate and classification of novae. *Mon. Not. R. Astron. Soc.* **183**, 515–522 (1978).
27. Aleksić, J. et al. The major upgrade of the MAGIC telescopes, part I: the hardware improvements and the commissioning of the system. *Astropart. Phys.* **72**, 61–75 (2016).
28. Aleksić, J. et al. The major upgrade of the MAGIC telescopes, part II: A performance study using observations of the Crab Nebula. *Astropart. Phys.* **72**, 76–94 (2016).
29. Zanin, R. et al. MARS, the MAGIC Analysis and Reconstruction Software. In *Proc. 33rd International Cosmic Ray Conference (ICRC)* (ed. Cintra Shellard, R.) 773 (Centro Brasileiro de Pesquisas Fisicas, 2013).
30. MAGIC Collaborationet al. VHE gamma-ray detection of FSRQ QSO B1420+326 and modeling of its enhanced broadband state in 2020. *Astron. Astrophys.* **647**, A163 (2021).
31. MAGIC Collaboration Teraelectronvolt emission from the γ-ray burst GRB 190114C. *Nature* **575**, 455–458 (2019).
32. Atwood, W. B. et al. The Large Area Telescope on the Fermi Gamma-Ray Space Telescope mission. *Astrophys. J.* **697**, 1071–1102 (2009).

33. Wood, M. et al. Fermipy: an open-source Python package for analysis of Fermi-LAT data. In *35th International Cosmic Ray Conference PoS(ICRC2017)* (ed. Park, H. et al.) 824 (International Cosmic Ray Conference Vol. 301, 2017).
34. Abdollahi, S. et al. Fermi Large Area Telescope fourth source catalog. *Astrophys. J. Suppl. Ser.* **247**, 33 (2020).
35. Ballet, J., Burnett, T. H., Digel, S. W. & Lott, B. Fermi Large Area Telescope fourth source catalog Data Release 2. Preprint at https://arxiv.org/abs/2005.11208 (2020).
36. Mattox, J. R. et al. The likelihood analysis of EGRET data. *Astrophys. J.* **461**, 396–407 (1996).
37. Principe, G., Malyshev, D., Ballet, J. & Funk, S. The first catalog of Fermi-LAT sources below 100 MeV. *Astron. Astrophys.* **618**, A22 (2018).
38. Nilsson, K. et al. Long-term optical monitoring of TeV emitting blazars. I. Data analysis. *Astron. Astrophys.* **620**, A185 (2018).
39. Munari, U. et al. The ANS Collaboration Monitoring Program. *Balt. Astron.* **21**, 13–21 (2012).
40. Munari, U. & Moretti, S. Characterizing the photometric response of the ANS Collaboration Monitoring Program. *Balt. Astron.* **21**, 22–31 (2012).
41. Henden, A. A., Levine, S. E., Terrell, D., Smith, T. C. & Welch, D. Data Release 3 of the AAVSO All-Sky Photometric Survey (APASS). *J. Am. Assoc. Var. Star Obs.* **40**, 430 (2012).
42. Henden, A. & Munari, U. The APASS all-sky, multi-epoch BVgri photometric survey. *Contrib. Astronom. Obs. Skalnate Pleso* **43**, 518–522 (2014).
43. Landolt, A. U. UBVRI photometric standard stars around the celestial equator: updates and additions. *Astron. J.* **137**, 4186–4269 (2009).
44. Munari, U., Henden, A., Frigo, A. & Dallaporta, S. APASS discovery and characterization of 180 variable stars in Aquarius. *J. Astron. Data* **20**, 4 (2014).
45. Munari, U. et al. APASS Landolt–Sloan BVgri photometry of RAVE stars. I. Data, effective temperatures, and reddenings. *Astron. J.* **148**, 81 (2014).
46. Teyssier, F. Eruptive stars monitoring and the ARAS database. *Contrib. Astron. Obs. Skalnate Pleso* **49**, 217–227 (2019).
47. Hachisu, I. & Kato, M. The UBV color evolution of classical novae. I. Nova–giant sequence in the color–color diagram. *Astrophys. J.* **785**, 97 (2014).
48. Cardelli, J. A., Clayton, G. C. & Mathis, J. S. The relationship between infrared, optical, and ultraviolet extinction. *Astrophys. J.* **345**, 245–256 (1989).
49. Bessell, M. S., Castelli, F. & Plez, B. Model atmospheres broad-band colors, bolometric corrections and temperature calibrations for O–M stars. *Astron. Astrophys.* **333**, 231–250 (1998).
50. Chesneau, O. et al. AMBER/VLTI interferometric observations of the recurrent nova RS Ophiuchii 5.5 days after outburst. *Astron. Astrophys.* **464**, 119–126 (2007).
51. Skopal, A. Multiwavelength modeling the SED of supersoft X-ray sources. II. RS Ophiuchi: from the explosion to the SSS phase. *New Astron.* **36**, 128–138 (2015).
52. Munari, U. & Valisa, P. The 2021 outburst of RS Oph. A pictorial atlas of the spectroscopic evolution: the first 18 days. Preprint at https://arxiv.org/abs/2109.01101 (2021).
53. Leone, F. et al. A method to calibrate the high-resolution Catania Astrophysical Observatory Spectropolarimeter. *Astron. J.* **151**, 116 (2016).
54. Catanzaro, G. et al. CAOS spectroscopy of Am stars Kepler targets. *Mon. Not. R. Astron. Soc.* **451**, 184–195 (2015).
55. Skopal, A., Pribulla, T., Buil, C., Vittone, A. & Errico, L. Non-spherical mass outflow from RS Ophiuchi during its 2006 outburst. In *RS Ophiuchi (2006) and the Recurrent Nova Phenomenon* (eds Evans, A. et al.) 227 (Astronomical Society of the Pacific Conference Series Vol. 401, 2008).
56. Mondal, A. et al. Optical spectroscopy of the recurrent nova RS Ophiuchi—from the outburst of 2006 to quiescence. *Mon. Not. R. Astron. Soc.* **474**, 4211–4224 (2018).
57. Ribeiro, V. A. R. M. et al. The expanding nebular remnant of the recurrent nova RS Ophiuchi (2006). II. Modeling of combined Hubble Space Telescope imaging and ground-based spectroscopy. *Astrophys. J.* **703**, 1955–1963 (2009).
58. Sokoloski, J. L., Rupen, M. P. & Mioduszewski, A. J. Uncovering the nature of nova jets: a radio image of highly collimated outflows from RS Ophiuchi. *Astrophys. J. Lett.* **685**, L137–L140 (2008).
59. Bode, M. F. et al. Hubble Space Telescope imaging of the expanding nebular remnant of the 2006 outburst of the recurrent nova RS Ophiuchi. *Astrophys. J. Lett.* **665**, 63–66 (2007).
60. Booth, R. A., Mohamed, S. & Podsiadlowski, P. Modelling the circumstellar medium in RS Ophiuchi and its link to type Ia supernovae. *Mon. Not. R. Astron. Soc.* **457**, 822–835 (2016).
61. Moderski, R., Sikora, M., Coppi, P. S. & Aharonian, F. Klein–Nishina effects in the spectra of non-thermal sources immersed in external radiation fields. *Mon. Not. R. Astron. Soc.* **363**, 954–966 (2005).
62. Walch, S. & Naab, T. The energy and momentum input of supernova explosions in structured and ionized molecular clouds. *Mon. Not. R. Astron. Soc.* **451**, 2757–2771 (2015).
63. Rozwadowska, K., Vissani, F. & Cappellaro, E. On the rate of core collapse supernovae in the Milky Way. *New Astron.* **83**, 101498 (2021).
64. Webber, W. R. A new estimate of the local interstellar energy density and ionization rate of Galactic cosmic rays. *Astrophys. J.* **506**, 329–334 (1998).
65. Buck, T., Pfrommer, C., Pakmor, R., Grand, R. J. J. & Springel, V. The effects of cosmic rays on the formation of Milky Way-mass galaxies in a cosmological context. *Mon. Not. R. Astron. Soc.* **497**, 1712–1737 (2020).
66. Schaefer, B. E. Orbital periods for three recurrent novae. *Astrophys. J.* **697**, 721–729 (2009).
67. Cheung, C. C. et al. Fermi-LAT gamma-ray detections of classical novae V1369 Centauri 2013 and V5668 Sagittarii 2015. *Astrophys. J.* **826**, 142 (2016).
68. Munari, U. et al. The 2006 outburst of the recurrent nova RS Oph. *Balt. Astron.* **16**, 46–48 (2007).

Acknowledgements

We thank the Instituto de Astrofísica de Canarias for the excellent working conditions at the Observatorio del Roque de los Muchachos in La Palma. The financial support of the German BMBF, MPG and HGF; the Italian INFN and INAF; the Swiss National Fund SNF; the ERDF under the Spanish Ministerio de Ciencia e Innovación (MICINN) (PID2019-104114RB-C31, PID2019-104114RB-C32, PID2019-104114RB-C33, PID2019-105510GB-C31,PID2019-107847RB-C41, PID2019-107847RB-C42, PID2019-107847RB-C44, PID2019-107988GB-C22); the Indian Department of Atomic Energy; the Japanese ICRR, the University of Tokyo, JSPS and MEXT; the Bulgarian Ministry of Education and Science, National RI Roadmap Project DO1-400/18.12.2020, and the Academy of Finland grant number 320045 is gratefully acknowledged. This work was also supported by the Spanish Centro de Excelencia Severo Ochoa (SEV-2016-0588, SEV-2017-0709, CEX2019-000920-S), the Unidad de Excelencia María de Maeztu (CEX2019-000918-M, MDM-2015-0509-18-2) and the CERCA programme of the Generalitat de Catalunya; by the Croatian Science Foundation (HrZZ) project IP-2016-06-9782 and the University of Rijeka Project uniri-prirod-18-48; by the DFG Collaborative Research Centres SFB823/C4 and SFB876/C3; by the Polish National Research Centre grant UMO-2016/22/M/ST9/00382 and by the Brazilian MCTIC, CNPq and FAPERJ. The TJO of the Montsec Observatory (OdM) is owned by the Catalan Government and operated by the Institute for Space Studies of Catalonia (IEEC). We acknowledge with thanks the variable star observations from the AAVSO International Database contributed by observers worldwide and used in this research. We gratefully acknowledge the prompt response to the alert and the data provided by the CAOS Team. We acknowledge with thanks the ARAS database[27] (https://aras-database.github.io/database/index.html). The observers who contributed worldwide data used in this research are O. Garde, V. Lecoq, L. Franco, F. Teyssier, O. Thizy, C. Boussin, P. A. Dubovsky and D. Boyd. We thank G. Principe for the advice in extending the Fermi LAT analysis below 100 MeV and F. D'Ammando for his comments on the manuscript. R.L.-C.'s work was financially supported by the European Union's Horizon 2020 research and innovation programme under the Marie Skłodowska-Curie grant agreement 754496—FELLINI.

Author contributions

The individual authors who contributed to this Letter, in alphabetic order, are W. Bednarek, theoretical interpretation; V.F.R., analysis and coordination of the optical photometry data, drafting of the corresponding paper section; D.G., triggering of the MAGIC observations, analysis of the MAGIC data, drafting and editing of the manuscript; F. Leone, coordination and analysis of the optical spectroscopy data, interpretation of ejecta kinematics; R.L.-C., analysis of the MAGIC and Fermi LAT data, theoretical interpretation, comparison with other novae, computation of the contribution to CRs, drafting and editing of the manuscript; A.L.-O., triggering and coordination of the MAGIC campaign, analysis of the MAGIC data, drafting and editing of the manuscript; U.M., analysis of the optical photometry data and cross-calibration of the different optical instruments; J. Sitarek, coordination of the MAGIC nova observation programme, analysis of the MAGIC data, theoretical modelling, leadership of the publication effort, drafting and editing of the manuscript; P.V., collection and analysis of the optical photometry data. The other authors have contributed in one or more of the following ways: design, construction, maintenance and operation of the instrument(s) used to acquire the data; preparation and/or evaluation of the observation proposals; data acquisition, processing, calibration and/or reduction; production of analysis tools and/or related Monte Carlo simulations; discussion and approval of the contents of the draft.

Competing interests

The authors declare no competing interests.

Additional information

Extended data is available for this paper at https://doi.org/10.1038/s41550-022-01640-z.

Supplementary information The online version contains supplementary material available at https://doi.org/10.1038/s41550-022-01640-z.

Correspondence and requests for materials should be addressed to D. Green, R. López-Coto, A. López-Oramas or J. Sitarek.

Peer review information *Nature Astronomy* thanks Joanna Mikolajewska and the other, anonymous, reviewer(s) for their contribution to the peer review of this work.

V. A. Acciari[1], S. Ansoldi[2,3], L. A. Antonelli[4], A. Arbet Engels[5], M. Artero[6], K. Asano[7], D. Baack[8], A. Babić[9], A. Baquero[10], U. Barres de Almeida[11], J. A. Barrio[10], I. Batković[12], J. Becerra González[1], W. Bednarek[13], L. Bellizzi[14], E. Bernardini[15], M. Bernardos[12], A. Berti[5], J. Besenrieder[5], W. Bhattacharyya[15], C. Bigongiari[4], A. Biland[16], O. Blanch[6], H. Bökenkamp[8], G. Bonnoli[17], Ž. Bošnjak[9], G. Busetto[12], R. Carosi[18], G. Ceribella[5], M. Cerruti[19], Y. Chai[5], A. Chilingarian[20], S. Cikota[9], S. M. Colak[6], E. Colombo[1], J. L. Contreras[10], J. Cortina[21], S. Covino[4], G. D'Amico[5,22], V. D'Elia[4], P. Da Vela[18,23], F. Dazzi[4], A. De Angelis[12], B. De Lotto[2], A. Del Popolo[24], M. Delfino[6,25], J. Delgado[6,25], C. Delgado Mendez[21], D. Depaoli[26], F. Di Pierro[26], L. Di Venere[27], E. Do Souto Espiñeira[6], D. Dominis Prester[28], A. Donini[2], D. Dorner[29], M. Doro[12], D. Elsaesser[8], V. Fallah Ramazani[30,31], L. Fariña Alonso[6], A. Fattorini[8], M. V. Fonseca[10], L. Font[32], C. Fruck[5], S. Fukami[16], Y. Fukazawa[33], R. J. García López[1], M. Garczarczyk[15], S. Gasparyan[34], M. Gaug[32], N. Giglietto[27], F. Giordano[27], P. Gliwny[13], N. Godinović[35], J. G. Green[5], D. Green[5] ✉, D. Hadasch[7], A. Hahn[5], T. Hassan[21], L. Heckmann[5], J. Herrera[1], J. Hoang[10,36], D. Hrupec[37], M. Hütten[7], T. Inada[7], K. Ishio[13], Y. Iwamura[7], I. Jiménez Martínez[21], J. Jormanainen[30], L. Jouvin[6], D. Kerszberg[6], Y. Kobayashi[7], H. Kubo[38], J. Kushida[39], A. Lamastra[4], D. Lelas[35], F. Leone[4], E. Lindfors[30], L. Linhoff[8], S. Lombardi[4], F. Longo[2,40], R. López-Coto[12] ✉, M. López-Moya[10], A. López-Oramas[1] ✉, S. Loporchio[27], B. Machado de Oliveira Fraga[11], C. Maggio[1,32], P. Majumdar[41], M. Makariev[42], M. Mallamaci[12], G. Maneva[42], M. Manganaro[28], K. Mannheim[29], L. Maraschi[4], M. Mariotti[12], M. Martínez[6], A. Mas Aguilar[10], D. Mazin[5,7], S. Menchiari[14], S. Mender[8], S. Mićanović[28], D. Miceli[2,43], T. Miener[10], J. M. Miranda[14], R. Mirzoyan[5], E. Molina[19], A. Moralejo[6], D. Morcuende[10], V. Moreno[1,32], E. Moretti[6], T. Nakamori[44], L. Nava[4], V. Neustroev[45], M. Nievas Rosillo[1], C. Nigro[6], K. Nilsson[30], K. Nishijima[39], K. Noda[7], S. Nozaki[38], Y. Ohtani[7], T. Oka[38], J. Otero-Santos[1], S. Paiano[4], M. Palatiello[2], D. Paneque[5], R. Paoletti[14], J. M. Paredes[19], L. Pavletić[28], P. Peñil[10], M. Persic[2,46], M. Pihet[5], P. G. Prada Moroni[18], E. Prandini[12], C. Priyadarshi[6], I. Puljak[35], W. Rhode[8], M. Ribó[19], J. Rico[6], C. Righi[4], A. Rugliancich[18], N. Sahakyan[34], T. Saito[7], S. Sakurai[7], K. Satalecka[15], F. G. Saturni[4], B. Schleicher[29], K. Schmidt[8], T. Schweizer[5], J. Sitarek[7] ✉, I. Šnidarić[47], D. Sobczynska[13], A. Spolon[12], A. Stamerra[4], J. Strišković[37], D. Strom[5], M. Strzys[7], Y. Suda[33], T. Surić[47], M. Takahashi[7], R. Takeishi[7], F. Tavecchio[4], P. Temnikov[42], T. Terzić[28], M. Teshima[5,7], L. Tosti[48], S. Truzzi[14], A. Tutone[4], S. Ubach[32], J. van Scherpenberg[5], G. Vanzo[1], M. Vazquez Acosta[1], S. Ventura[14], V. Verguilov[42], C. F. Vigorito[26], V. Vitale[49], I. Vovk[7], M. Will[5], C. Wunderlich[14], T. Yamamoto[50], D. Zarić[35], F. Ambrosino[51], M. Cecconi[52], G. Catanzaro[53], C. Ferrara[53], A. Frasca[53], M. Munari[53], L. Giustolisi[53], J. Alonso-Santiago[53], M. Giarrusso[54], U. Munari[55] and P. Valisa[56]

[1]Instituto de Astrofísica de Canarias and Departamento de Astrofísica, Universidad de La Laguna, La Laguna, Spain. [2]Università di Udine and INFN Trieste, Udine, Italy. [3]International Center for Relativistic Astrophysics (ICRA), Rome, Italy. [4]National Institute for Astrophysics (INAF), Rome, Italy. [5]Max-Planck-Institut für Physik, Munich, Germany. [6]Institut de Física d'Altes Energies (IFAE), The Barcelona Institute of Science and Technology (BIST), Barcelona, Spain. [7]Japanese MAGIC Group: Institute for Cosmic Ray Research (ICRR), The University of Tokyo, Kashiwa, Japan. [8]Technische Universität Dortmund, Dortmund, Germany. [9]Croatian MAGIC Group: University of Zagreb Faculty of Electrical Engineering and Computing (FER), Zagreb, Croatia. [10]IPARCOS Institute and EMFTEL Department, Universidad Complutense de Madrid, Madrid, Spain. [11]Centro Brasileiro de Pesquisas Físicas (CBPF), Rio de Janeiro, Brazil. [12]Università di Padova and INFN, Padua, Italy. [13]Department of Astrophysics, Faculty of Physics and Applied Informatics, University of Lodz, Lodz, Poland. [14]Università di Siena and INFN Pisa, Siena, Italy. [15]Deutsches Elektronen-Synchrotron (DESY), Zeuthen, Germany. [16]ETH Zürich, Zurich, Switzerland. [17]Instituto de Astrofísica de Andalucía-CSIC, Granada, Spain. [18]Università di Pisa and INFN Pisa, Pisa, Italy. [19]Universitat de Barcelona, ICCUB, IEEC-UB, Barcelona, Spain. [20]Armenian MAGIC Group: A. Alikhanyan National Science Laboratory, Yerevan, Armenia. [21]Centro de Investigaciones Energéticas, Medioambientales y Tecnológicas, Madrid, Spain. [22]Department for Physics and Technology, University of Bergen, Bergen, Norway. [23]University of Innsbruck, Innsbruck, Austria. [24]INFN MAGIC Group: INFN Sezione di Catania and Dipartimento di Fisica e Astronomia, University of Catania, Catania, Italy. [25]Port d'Informació Científica (PIC), Barcelona, Spain. [26]INFN MAGIC Group: INFN Sezione di Torino and Università degli Studi di Torino, Turin, Italy. [27]INFN MAGIC Group: INFN Sezione di Bari and Dipartimento Interateneo di Fisica dell'Università e del Politecnico di Bari, Bari, Italy. [28]Croatian MAGIC

Group: University of Rijeka Department of Physics, Rijeka, Croatia. [29]Universität Würzburg, Würzburg, Germany. [30]Finnish MAGIC Group: Finnish Centre for Astronomy with ESO, University of Turku, Turku, Finland. [31]Fakultät für Physik und Astronomie, Astronomisches Institut Ruhr-Universität Bochum (AIRUB), Bochum, Germany. [32]Departament de Física, and CERES-IEEC, Universitat Autònoma de Barcelona, Bellaterra, Spain. [33]Japanese MAGIC Group: Physics Program, Graduate School of Advanced Science and Engineering, Hiroshima University, Hiroshima, Japan. [34]Armenian MAGIC Group: ICRANet-Armenia at NAS RA, Yerevan, Armenia. [35]Croatian MAGIC Group: University of Split, Faculty of Electrical Engineering, Mechanical Engineering and Naval Architecture (FESB), Split, Croatia. [36]Department of Astronomy, University of California Berkeley, Berkeley, CA, USA. [37]Croatian MAGIC Group: Josip Juraj Strossmayer University of Osijek, Department of Physics, Osijek, Croatia. [38]Japanese MAGIC Group: Department of Physics, Kyoto University, Kyoto, Japan. [39]Japanese MAGIC Group: Department of Physics, Tokai University, Hiratsuka, Japan. [40]Dipartimento di Fisica, Università di Trieste, Trieste, Italy. [41]Saha Institute of Nuclear Physics, HBNI, Kolkata, India. [42]Institute for Nuclear Research and Nuclear Energy, Bulgarian Academy of Sciences, Sofia, Bulgaria. [43]Laboratoire d'Annecy de Physique des Particules (LAPP), CNRS-IN2P3, Annecy, France. [44]Japanese MAGIC Group: Department of Physics, Yamagata University, Yamagata, Japan. [45]Finnish MAGIC Group: Astronomy Research Unit, University of Oulu, Oulu, Finland. [46]INAF Trieste and Department of Physics and Astronomy, University of Bologna, Bologna, Italy. [47]Croatian MAGIC Group: Ruđer Bošković Institute, Zagreb, Croatia. [48]INFN MAGIC Group: INFN Sezione di Perugia, Perugia, Italy. [49]INFN MAGIC Group: INFN Roma Tor Vergata, Roma, Italy. [50]Japanese MAGIC Group: Department of Physics, Konan University, Kobe, Japan. [51]INAF—Osservatorio Astrofisico di Roma, Rome, Italy. [52]INAF—Fundacion Galileo Galilei, Breña Baja, Spain. [53]INAF—Osservatorio Astrofisico di Catania, Catania, Italy. [54]INFN—Laboratori Nazionali del Sud, Catania, Italy. [55]INAF—Osservatorio Astronomico di Padova, Asiago, Italy. [56]ANS Collaboration, c/o Astronomical Observatory, Asiago, Italy. ✉e-mail: damgreen@mpp.mpg.de; rlopezcoto@gmail.com; aloramas@iac.es; jsitarek@uni.lodz.pl

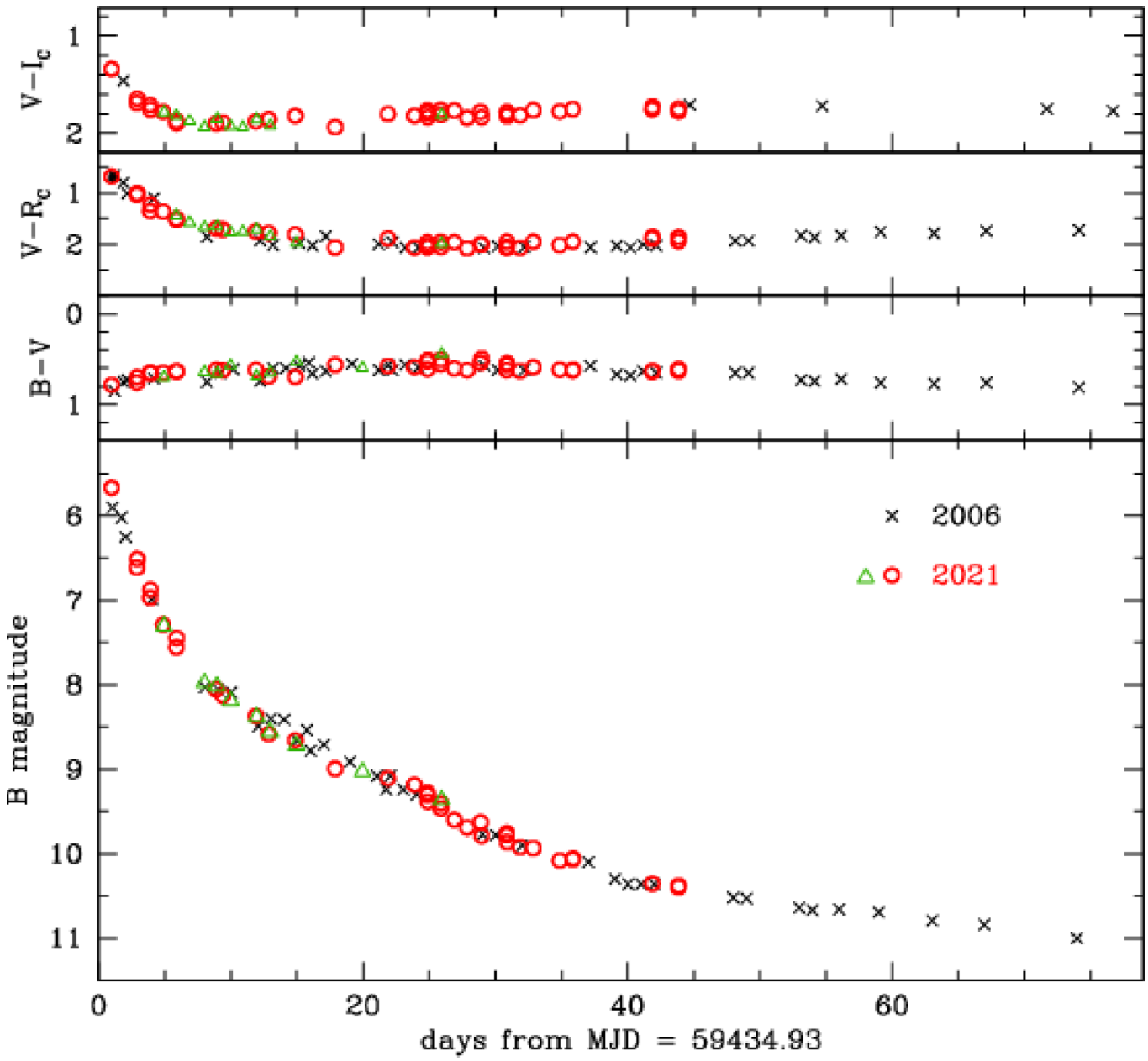

Extended Data Fig. 1 | Optical B-band observed magnitude and the color index of RS Oph 2021 outburst from ANS and TJO compared to that of 2006 eruption. Optical B-band observed magnitude and the color index of RS Oph 2021 outburst from ANS (red circles) and TJO (green triangle) compared to that of 2006 eruption (black crosses, computed with respect to MJD of 53775.86, [70]). Top three panels show the color indices, while the bottom panel shows B magnitude evolution.

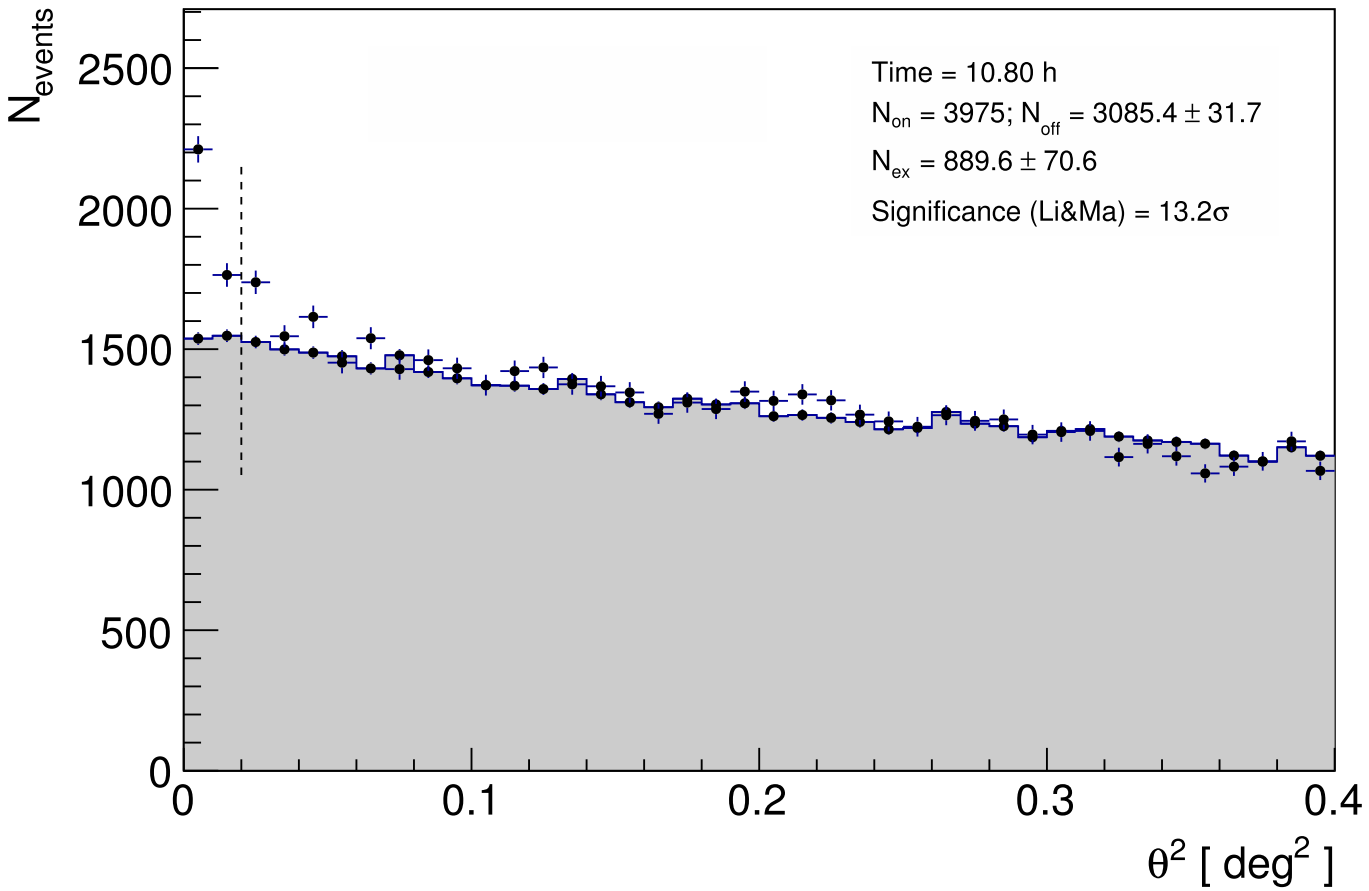

Extended Data Fig. 2 | Distribution of the squared angular distance between the nominal source position and the reconstructed arrival direction of events and the estimated background. Distribution of the squared angular distance between the nominal source position and the reconstructed arrival direction of events (black crosses) and the estimated background (gray shaded area). Vertical dashed line represents the angular cut below which the number of background and excess events as well as the statistical significance of the detection are given (inset panel). Error bars represent 1-sigma statistical uncertainties in the data points.

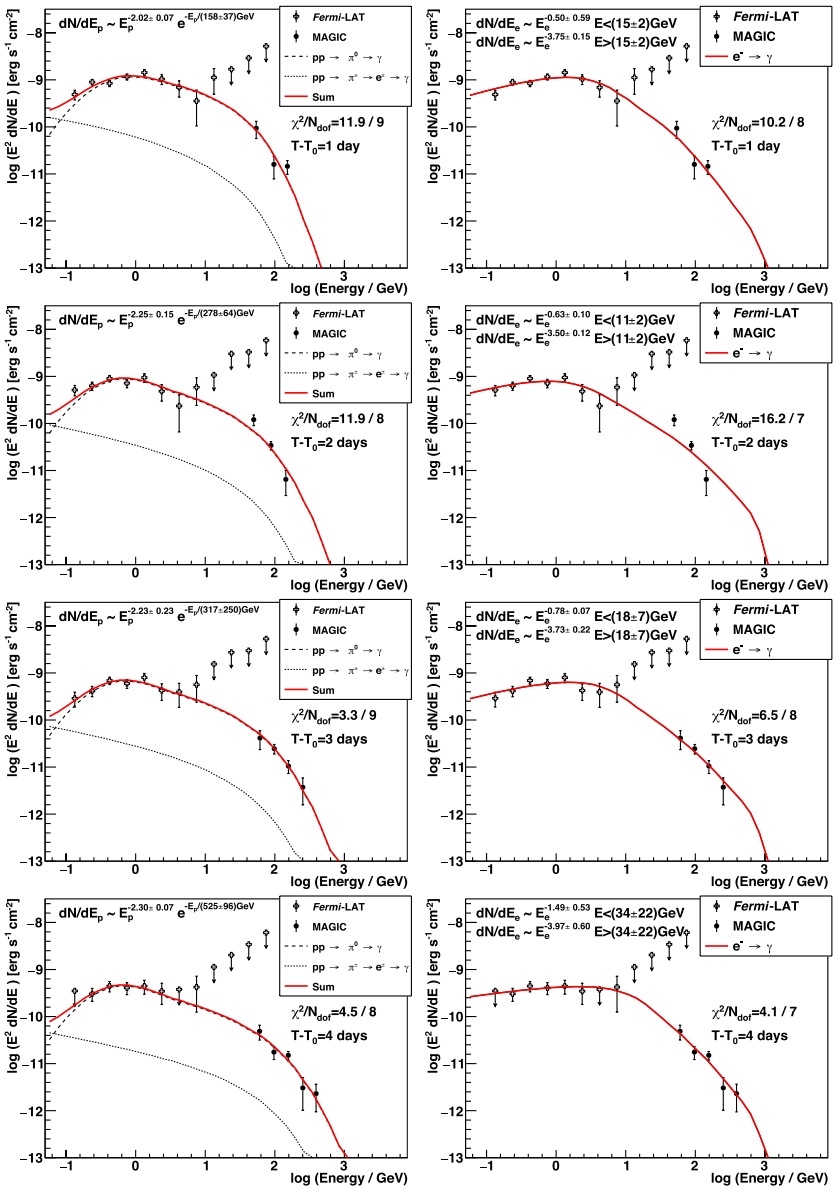

Extended Data Fig. 3 | Modeling of daily emission in proton model and electron model for first, second, third and fourth day after the nova eruption. Modeling of daily emission in proton model (left panels) and electron model (right panels) for first, second, third and fourth day after the nova eruption (from top to bottom). The dashed line shows the gamma rays from the π^0 decay and the dotted line shows the inverse Compton contribution of the secondary e ± pairs produced in hadronic interactions. dN/dE p and dN/dEe report the shape of the proton and electron energy distributions obtained from the fit. The bottom panel shows the fit residuals. Error bars represent 1-sigma statistical uncertainties in the data points.

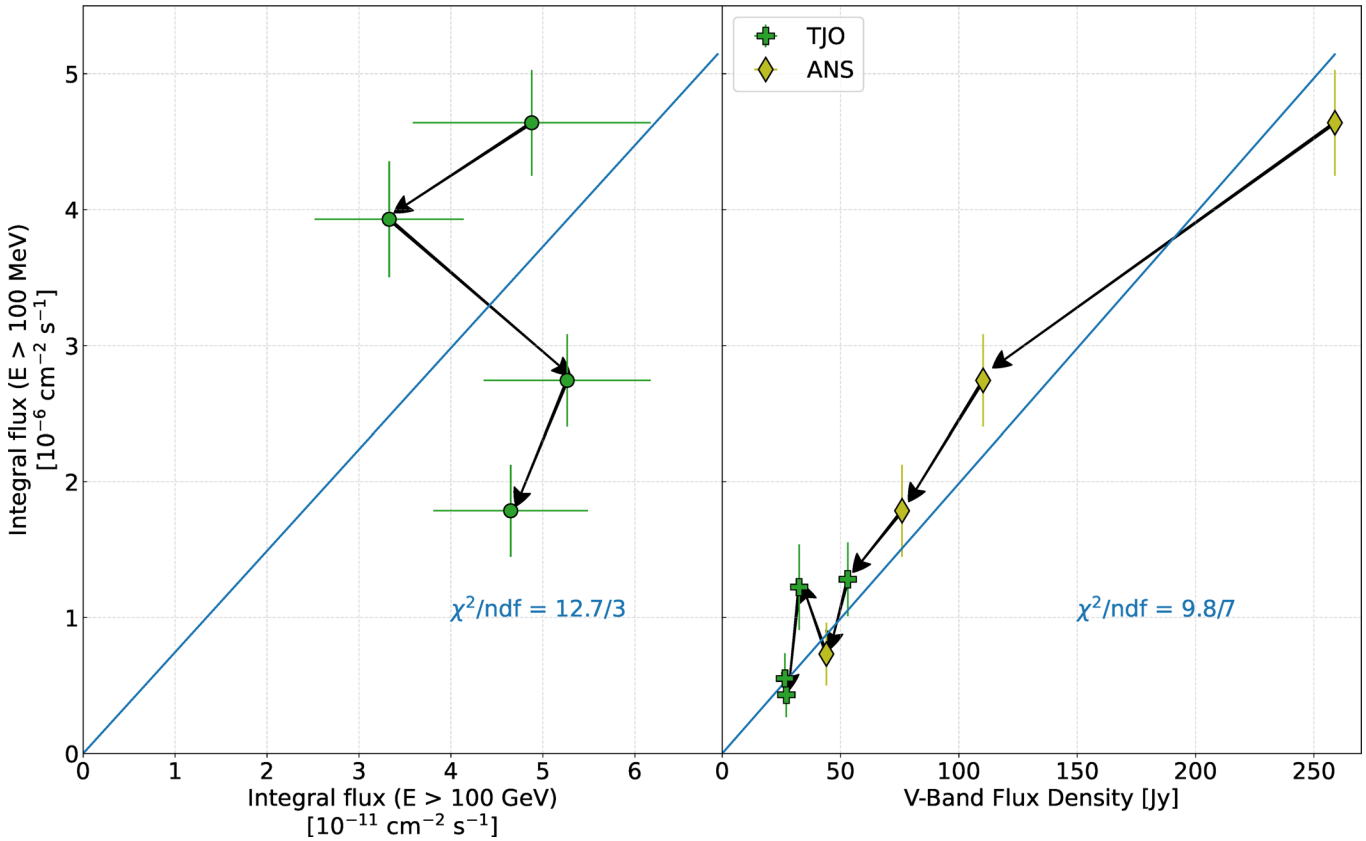

Extended Data Fig. 4 | Comparison of the photon flux measured by Fermi LAT above 100 MeV with the one measured by MAGIC above 100 GeV and with that of the V -band obtained by ANS. Comparison of the photon flux measured by Fermi LAT above 100 MeV with the one measured by MAGIC above 100 GeV (left panel) and with that of the V band obtained by ANS (right panel). Arrows show the sequence of the flux temporal evolution and the blue line shows the linear proportionality fit in both panels. Error bars represent 1-sigma statistical uncertainties in the data points.

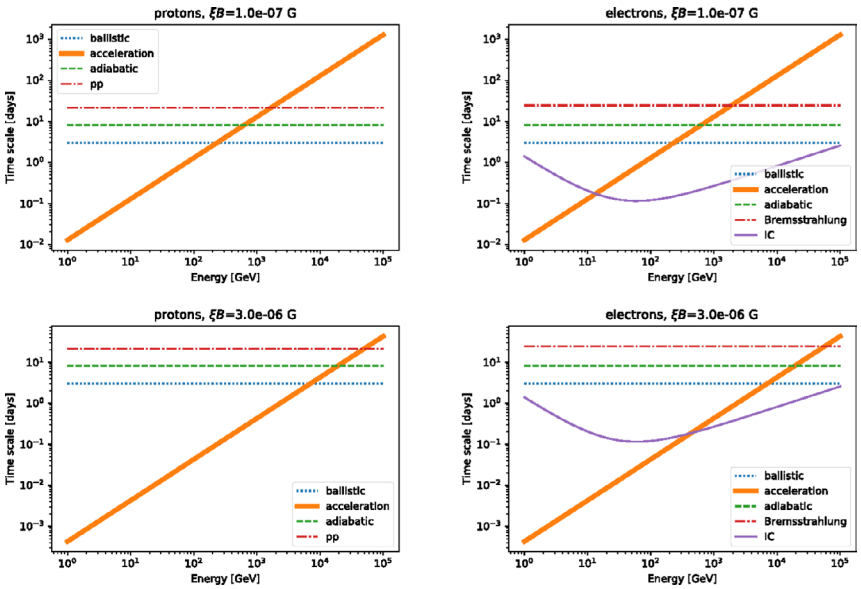

Extended Data Fig. 5 | Cooling and acceleration time scale for protons and electrons. Cooling and acceleration time scale for protons (left panels) and electrons (right panels) for two values of ξB parameter: 10^{-7} G (top panels) and 3×10^{-6} G (bottom panels). Assumed parameters (see text for details): $v_{sh} = 4500$ km s^{-1}, t = 3 d, $R_{ph} = 200$ R, $T_{ph} = 8460$ K, $n_p = 6\times10^8$ cm^{-3}.

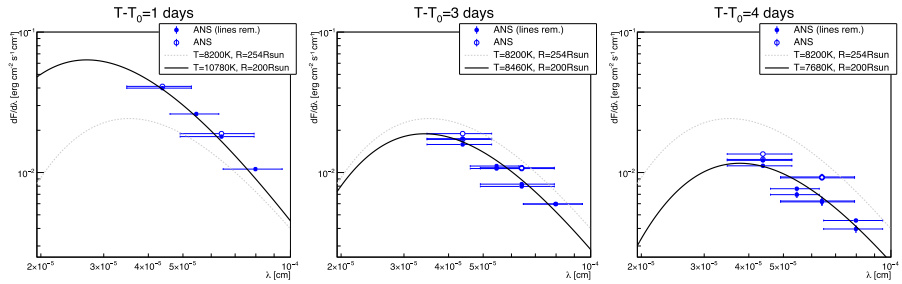

Extended Data Fig. 6 | Optical photometry performed by ANS 1, 3, and 4 days after the outburst. Optical photometry performed by ANS 1, 3, and 4 days (see the panel titles) after the outburst (blue empty markers) corrected for the Galactic absorption. Filled markers show the flux after subtraction of Hα and Hß line contributions. The thick black lines show a black-body emission used in the modeling, while the dashed line shows for comparison the average 2006 spectral fit from [52] (with the photosphere radius corrected to the distance of 2.45 kpc). Horizontal error bars represent the bandwidth of the filters used.

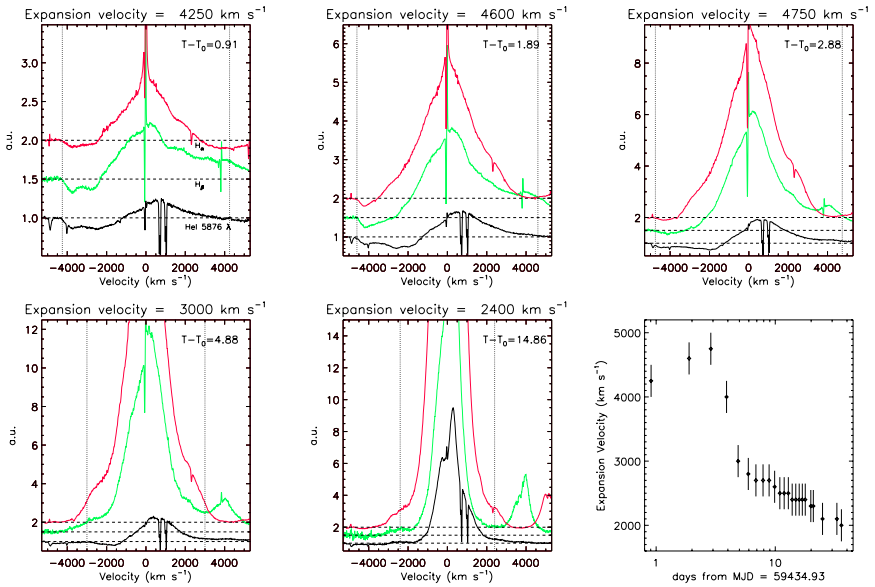

Extended Data Fig. 7 | Example of H α, H β and He I λ5876 P Cygni profiles used to determine the behavior of the expansion velocity of the expanding envelope. Example of H α, H β and He I 5876λ P Cygni profiles used to determine the behavior of the expansion velocity of the expanding envelope time after the outburst is given in the top right part of each panel). The bottom right panel shows the evolution of the velocity in time. Error bars represent 1-sigma statistical uncertainties in the data points.

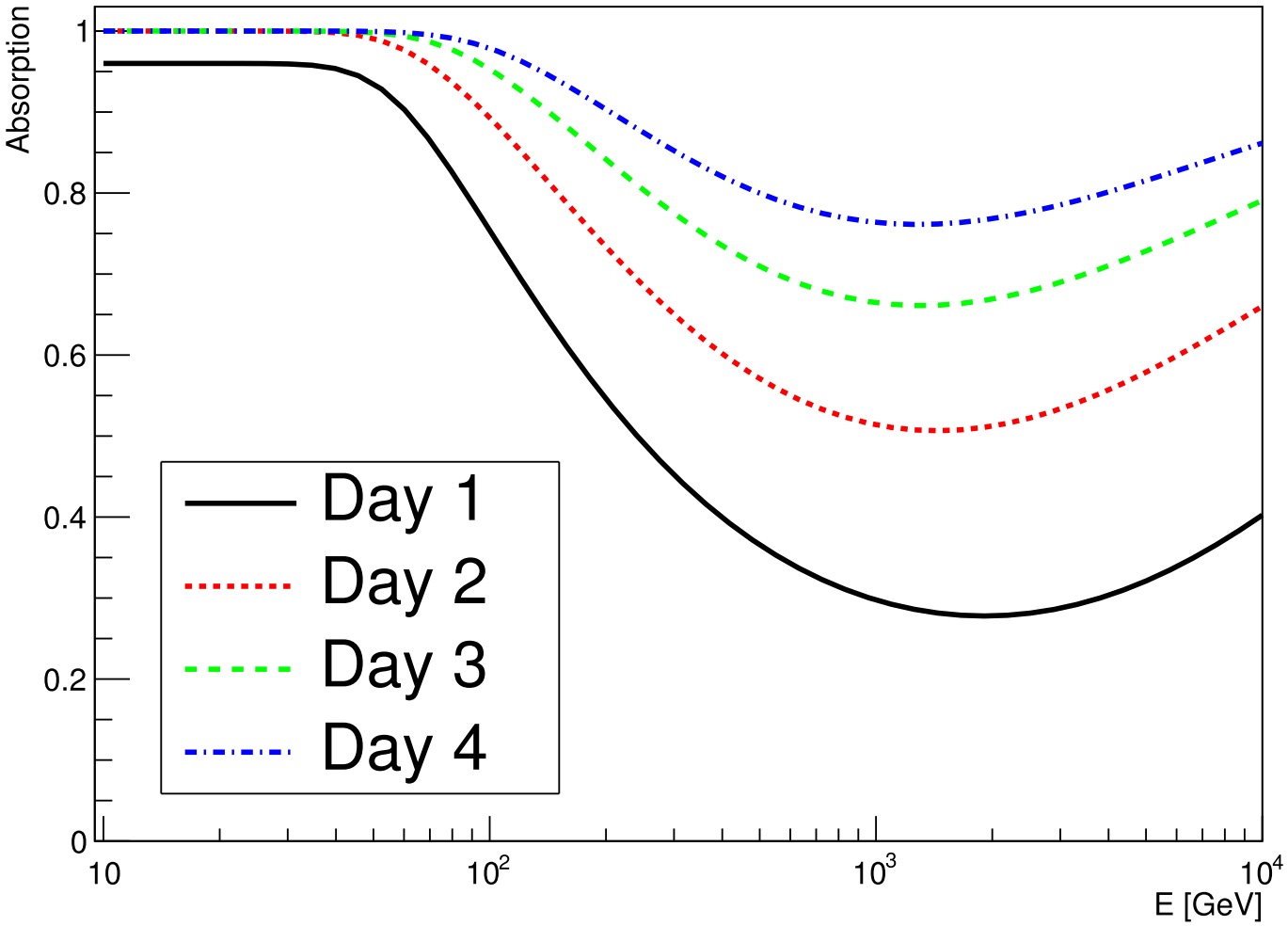

Extended Data Fig. 8 | Absorption of the gamma-ray emission on the radiation field of the photosphere and collision with it. Assumed parameters: v_{sh} = 4500 km s^{-1}, R_{ph} = 200 R. Temperature of the photosphere is T_{ph} = 10780 K, 9490 K, 8460 K and 7680 K for the time after the nova onset: 1 d (black solid), 2 d (red dotted), 3 d (green dashed), 4 d (blue dot-dashed) respectively.

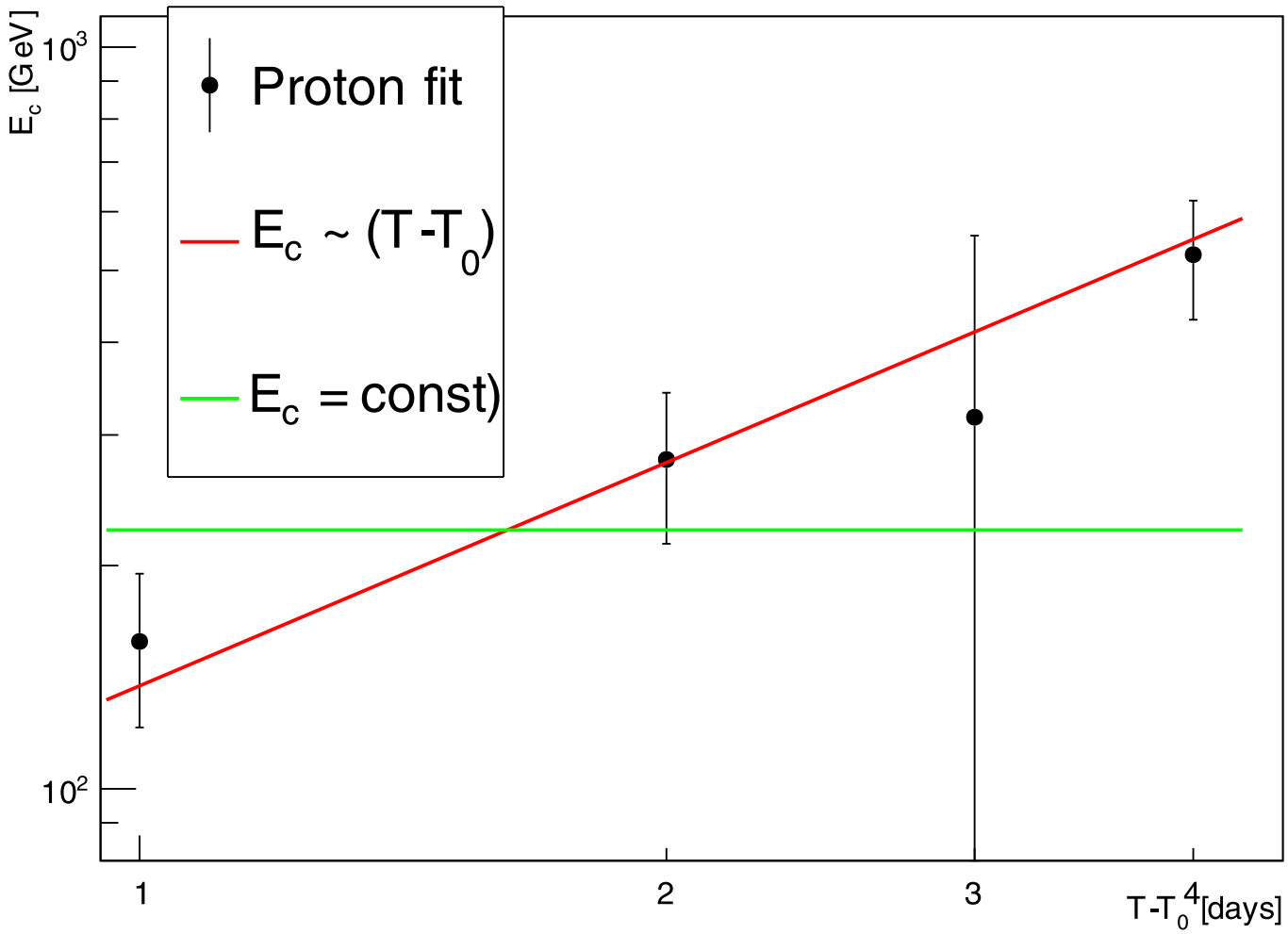

Extended Data Fig. 9 | The maximum energy of protons obtained from the theoretical model fits to the daily gamma-ray emission. The maximum energy of protons obtained from the theoretical model fits to the daily gamma-ray emission (points) shown in Fig. 3. Red and green line show, respectively, the scenario of proportional increase and constant value of maximum energy. Error bars represent 1-sigma statistical uncertainties in the determination of the maximum energy of protons.

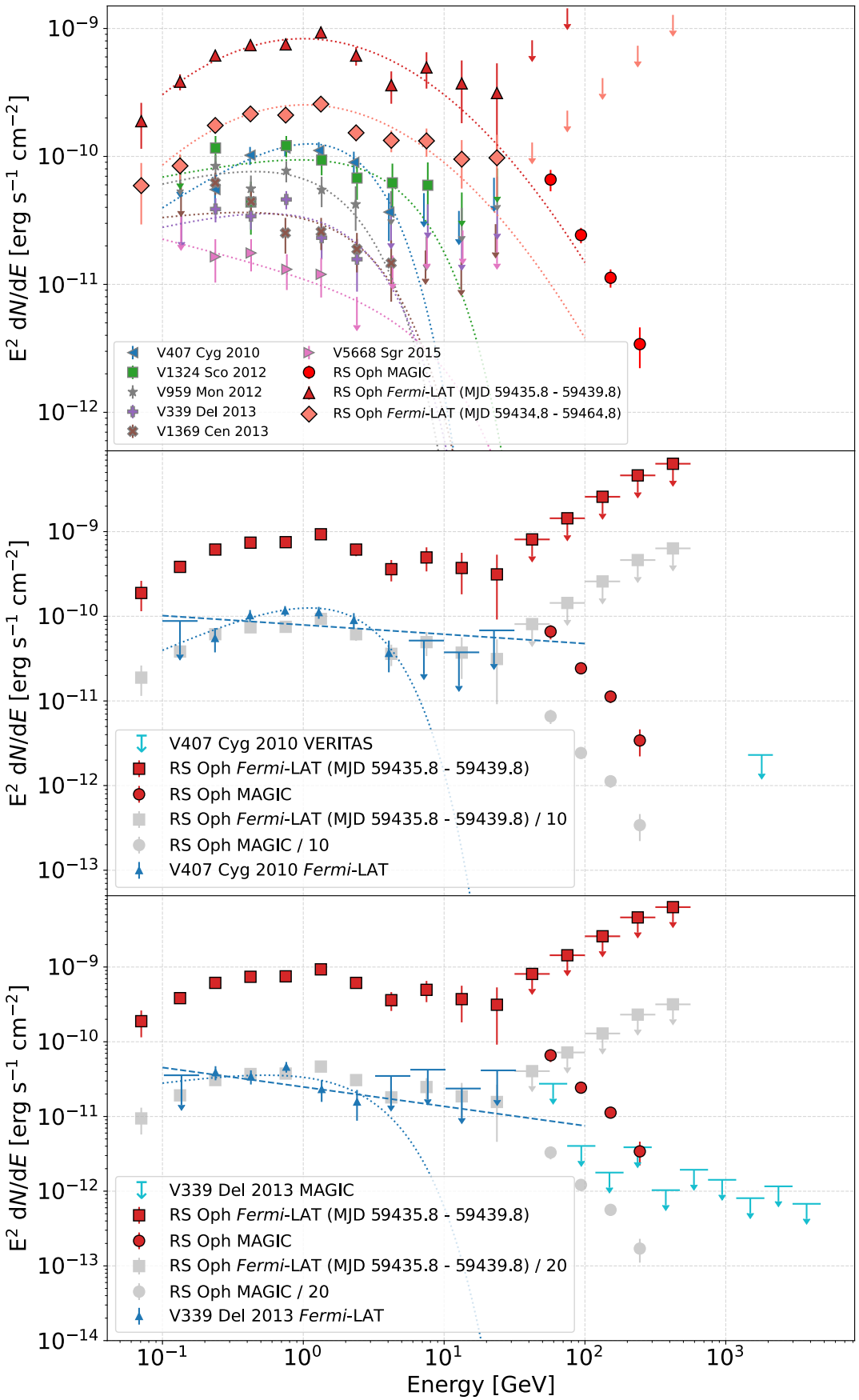

Extended Data Fig. 10 | See next page for caption.

Extended Data Fig. 10 | Comparison of RS Oph to other Fermi-LAT-detected novae. Spectra of other Fermi-LAT-detected novae are shown in the top panel. Gamma-ray spectra of V407 Cyg (middle panel) and V339 Del (bottom panel) compared to the measured (red) and scaled (gray) RS Oph gamma-ray spectra. Blue triangles and arrows correspond to *Fermi*-LAT measurements and upper limits of V407 Cyg (top) and V339 Del (bottom). Red squares are the Fermi-LAT spectrum of RS Oph and red circles the MAGIC one. Gray squares are the *Fermi*-LAT scaled spectrum of RS Oph and gray circles the MAGIC one. Cyan arrows correspond to the VERITAS (V407 Cyg) and MAGIC (V339 Del) upper limits. The dashed blue lines correspond to the best-fit using a single power-law for the *Fermi*-LAT data. The dotted blue lines correspond to the best-fit using a power-law with an exponential cut-off for the *Fermi*-LAT data. Data taken from[13–16,68]. Error bars represent 1-sigma statistical uncertainties in the data points.